Universitat Autònoma
de Barcelona

Design and characterization of dense and porous Fe-based alloys for biomedical and environmental applications

Yuping Feng

Tesi Doctoral

Programa de Doctorat en Ciència de Materials

Jordi Sort Viñas (director i tutor)

Eva Pellicer Vilà (directora)

Jordina Fornell Beringues (directora)

Departament de Física

Facultat de Ciències

2017

Supporting Information

Nanoporous Fe-based alloy prepared by selective dissolution: an effective Fenton catalyst for water remediation

Huiyan Zhang[a], *Yuping Feng*[a], *Yangyang Cheng*[b], *Maria D. Baró*[a], *Ainhoa Altube*[c], *Eva García-Lecina*[c], *Francisco Alcaide*[d], *Eva Pellicer*[a,*], *Tao Zhang*[b], *Jordi Sort*[a,e,§]

[a] Departament de Física, Building Cc, Universitat Autònoma de Barcelona, Bellaterra, Barcelona, E08193, Spain.

[b] Key Laboratory of Aerospace Materials and Performance (Ministry of Education), School of Materials Science and Engineering, Beihang University, 37 Xueyuanlu, Haidian District, Beijing, 100191, China.

[c] Unidad de Superficies Metálicas, IK4-CIDETEC, Paseo Miramón 196, Donostia-San Sebastián, Gipuzkoa, E20009, Spain.

[d] Unidad de Nuevas Tecnologías para la Energía, IK4-CIDETEC, Paseo Miramón 196, Donostia-San Sebastián, Gipuzkoa, E20009, Spain.

[e] Institució Catalana de Recerca i Estudis Avançats (ICREA), Passeig Lluís Companys 23, E08010 Barcelona, Spain.

To whom correspondence should be addressed: *eva.pellicer@uab.cat; §jordi.sort@uab.cat

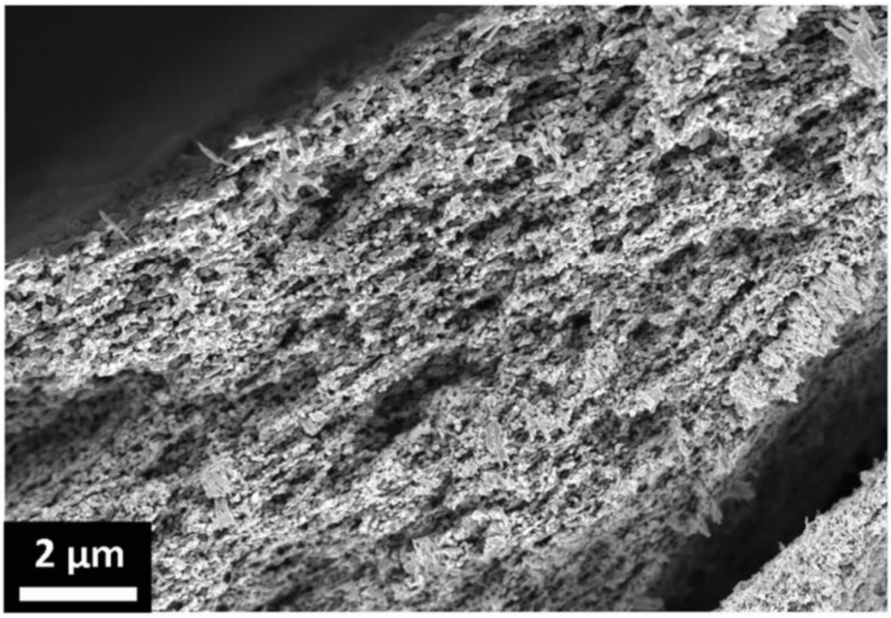

Figure S1. SEM image of the fracture cross section of the dealloyed ribbon at low magnification. A fully porous morphology can be appreciated.

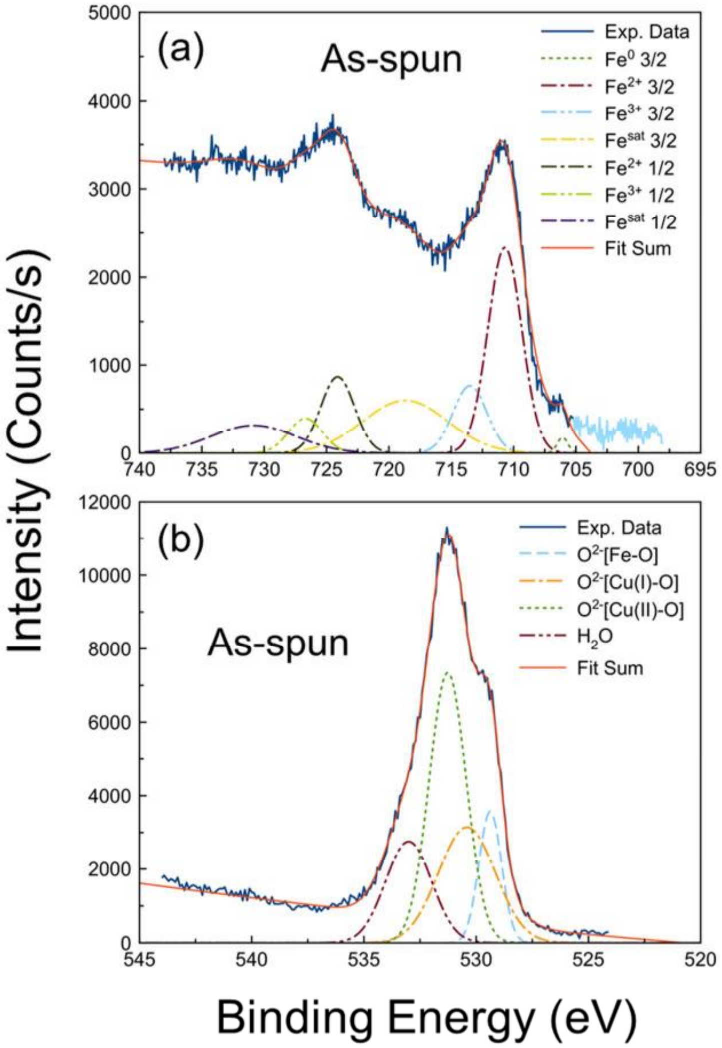

Figure S2. Experimental and deconvoluted (a) Fe 2p and (b) O 1s high resolution XPS spectra of as-spun $Fe_{43.5}Cu_{56.5}$ ribbon at surface level.

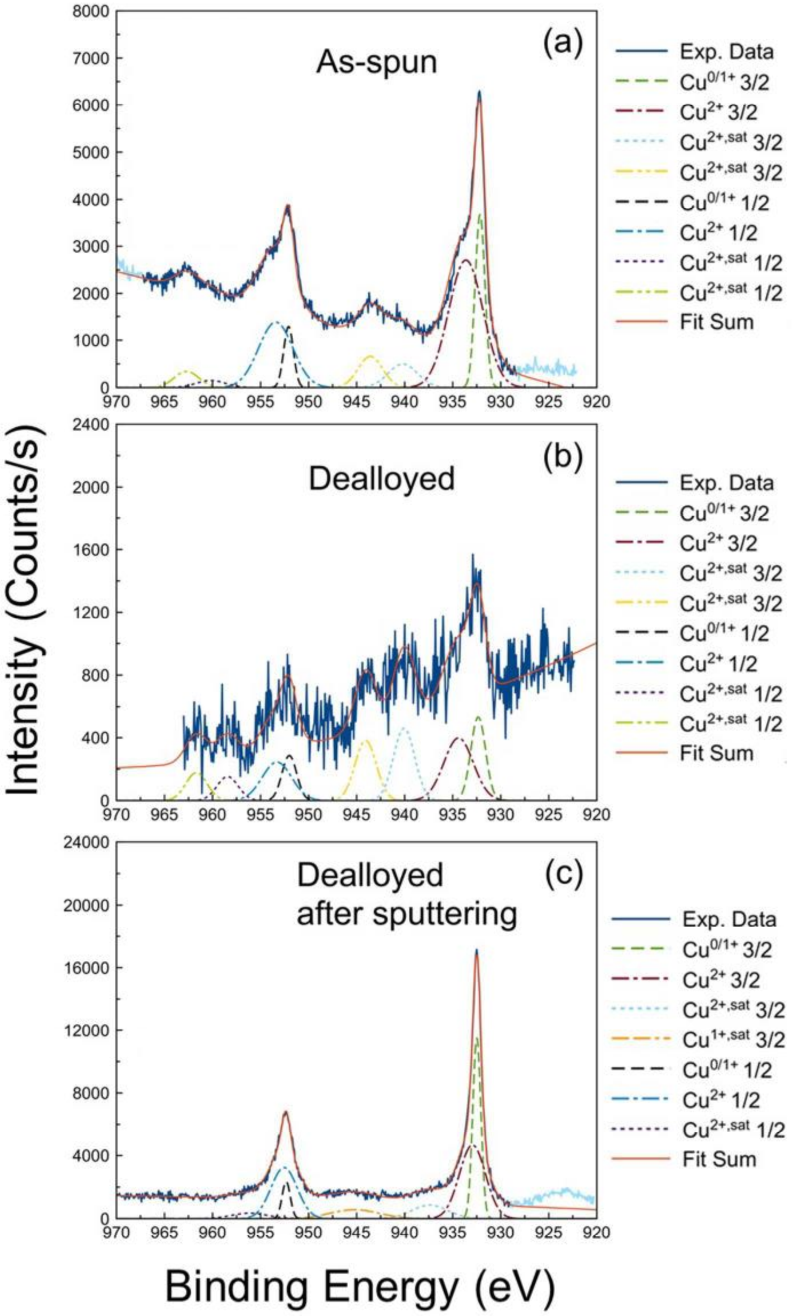

Figure S3. Experimental and deconvoluted Cu 2p high resolution XPS spectra taken on (a) the as-spun ribbon at surface level, and the dealloyed ribbon at (b) surface level and (c) after 1 min Ar ions sputtering.

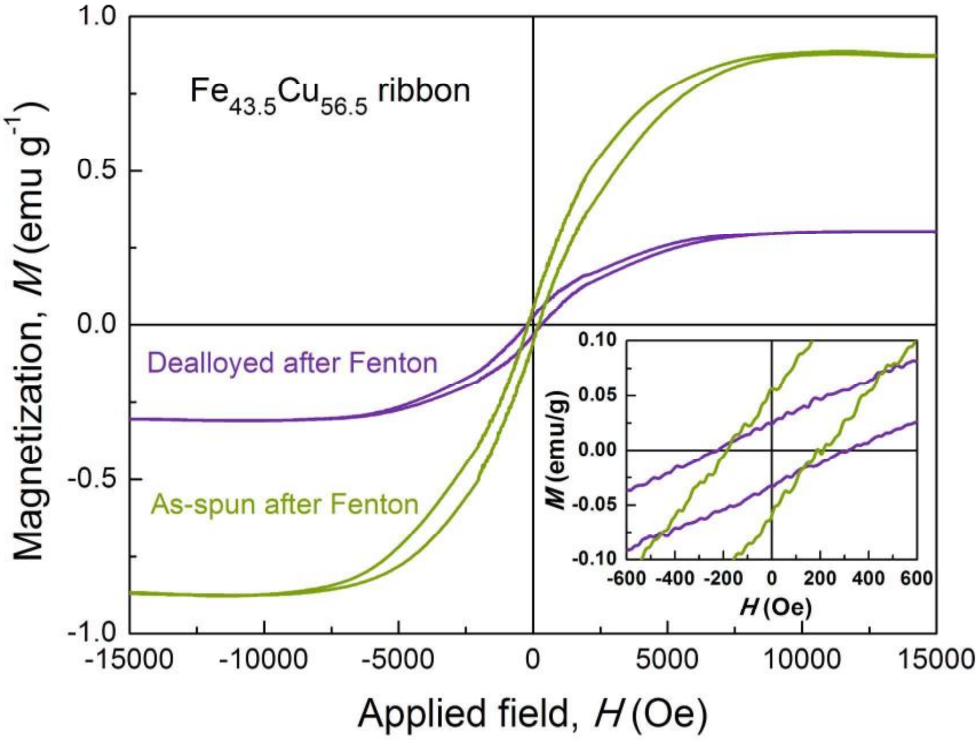

Figure S4. Hysteresis loops of as-spun and dealloyed ribbons after Fenton reaction. The inset shows magnified view at low fields.

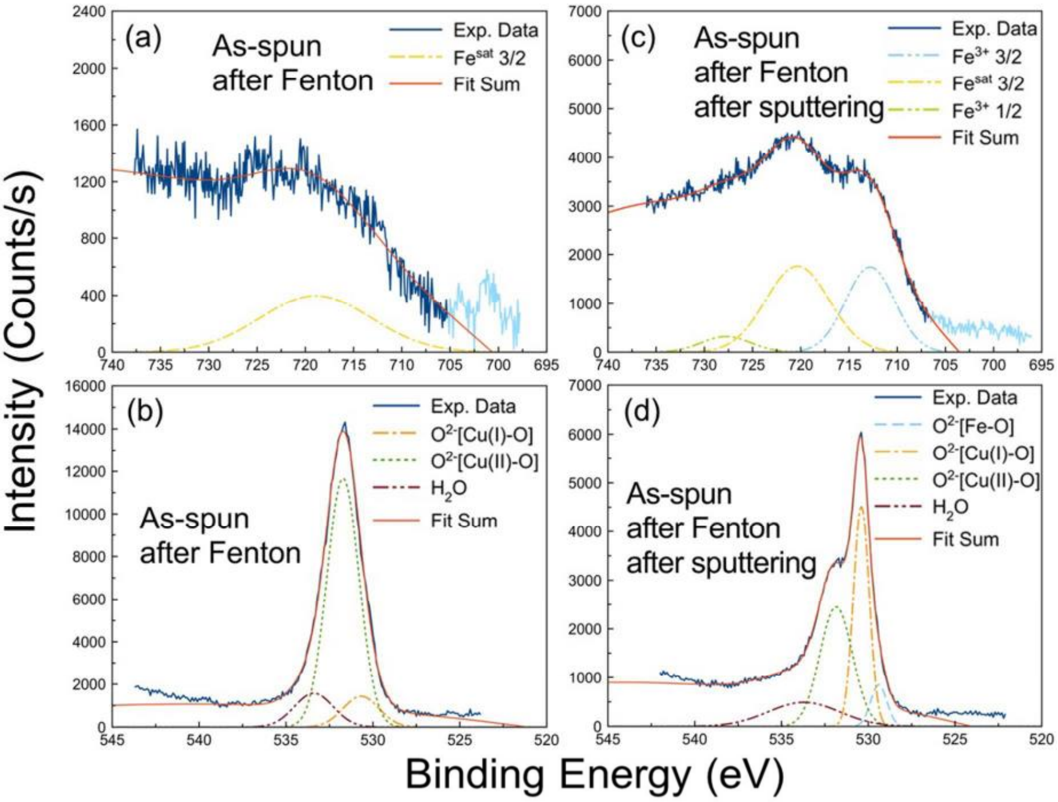

Figure S5. Experimental and deconvoluted high resolution XPS spectra for as-spun ribbon after Fenton reaction: (a) Fe 2p and (b) O 1s at surface level, and (c) Fe 2p and (d) O 1s after 1 min Ar ions sputtering.

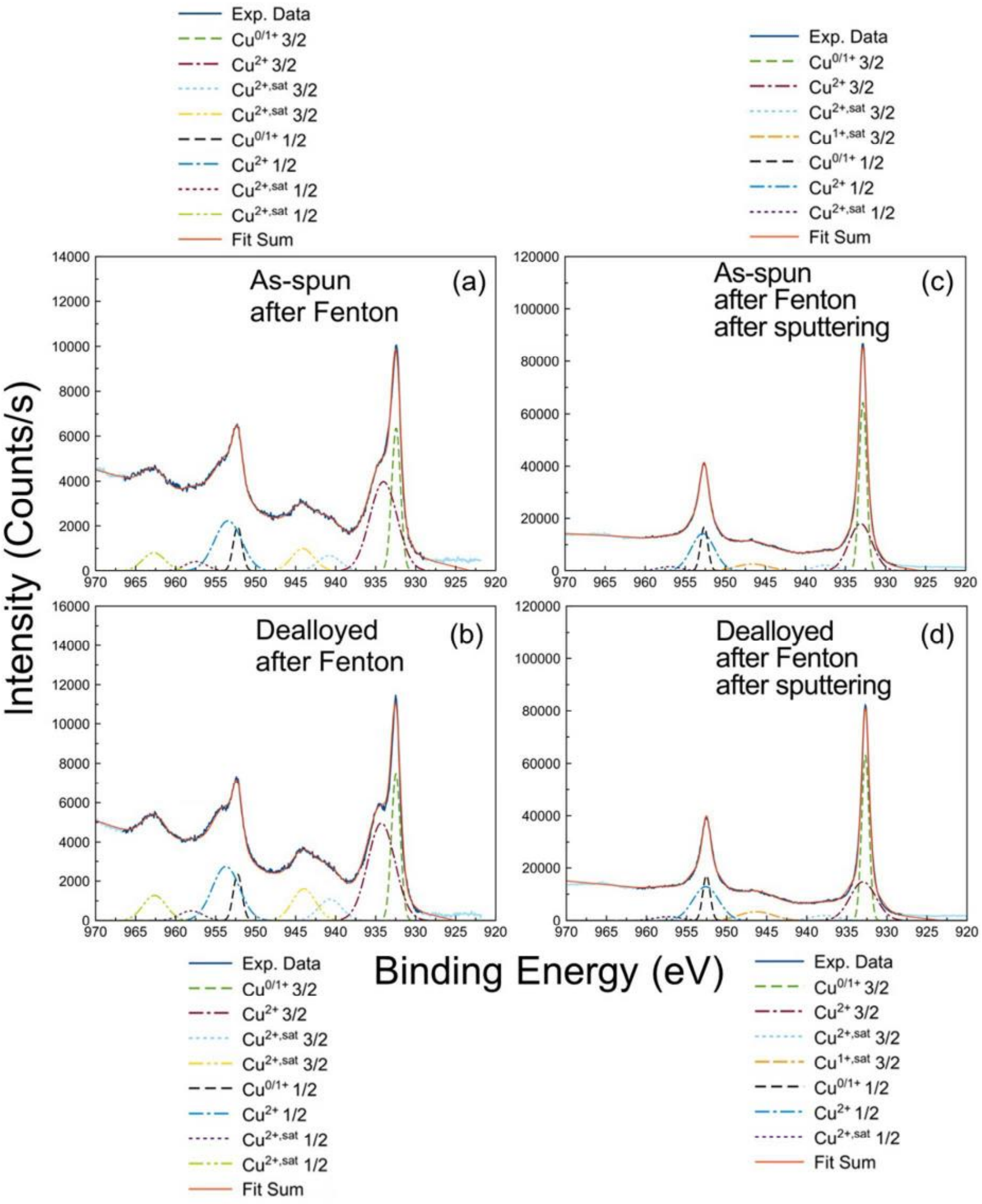

Figure S6. Experimental and deconvoluted Cu 2p high resolution XPS spectra of (a) surface and (b) after 1 min sputtering of as-spun ribbon after Fenton reaction, as well as of (c) surface and (d) after 1 min sputtering of dealloyed ribbon after Fenton reaction.

3.4 Sub-micron magnetic patterns and local variations of adhesion force induced in non-ferromagnetic amorphous Steel by femtosecond pulsed laser irradiation

In this article, we provide the first experimental demonstration that femtosecond pulsed laser irradiation (FSPLI) can be used as a direct, fast and inexpensive method to create periodic magnetic patterns at the surface of a non-ferromagnetic alloy. Besides the formation of ferromagnetic low-spatial-frequency ripples, much smaller nanoripples (of a few tens of nm in lateral size) are also generated during the FSPLI process, which is consistent with the coupling of the incident electromagnetic radiation with plasmon charge oscillations, as reported by several theoretical works in the literature. Such nanoripples are clearly observed by high-resolution SEM and AFM and give rise to local variations of the adhesion force during AFM scanning.

Traditionally, sophisticated lithographic procedures for magnetic patterning, that are usually rather time-consuming (i.e., consisting of multiple steps) and costly (i.e., requiring clean room facilities), are utilized to fabricate arrays of ferromagnetic dots. In the last few years, some non-conventional approaches for the direct magnetic patterning of initially non-magnetic materials have been developed; for example, ion irradiation or nanoindentation. Nevertheless, ion irradiation requires the use of a pre-lithographed shadow mask, while nanoindentation is a time-consuming technique (it takes about 1-2 min to perform a single indentation impression). Conversely, inducing magnetic patterning by FSPLI in a 1 cm^2 region of material requires only about 10 seconds. This is orders of magnitude less in time compared to nanoindentation (indeed, about 2-3 hours are needed to fabricate an array of magnetic dots covering the same area by nanoindentation).

The origin of the observed ferromagnetism is the FSPLI-induced surface devitrification of non-magnetic Fe-based amorphous steel. Among the various generated crystalline phases are: ferromagnetic α-Fe and Fe_3C, and ferrimagnetic $(Fe,Mn)_3O_4$ and Fe_2CrO_4. The generation of magnetic structures by FSPLI turns out to be one of the fastest ways to induce magnetic patterning without the need of any shadow mask. Furthermore, the observed variations in adhesion force can be particularly important for certain applications like traps for magnetic nanoparticles, where an exceedingly hydrophobic surface would not be desirable.

The hardness decreases from H_B = 14 GPa to H_B = 9.5 GPa after FSPLI. Similarly, E_r decreases from 193 to 83 GPa. Such variations of surface mechanical properties can be ascribed to the increase of surface roughness caused by the laser irradiation. The occurrence of roughness and surface corrugation is known to also play a crucial role in the hydrophobicity properties of surfaces. Here an increase of contact angle, from 64° to 75° is observed after FSPLI. This increase is quite modest compared to the results obtained from other rougher surfaces prepared by different methods. Namely, certain FSPLI conditions can render superhydrophobic surfaces by adjusting both the topological damage as well as the composition of the alloy at surface level.

These effects are of interest for applications (e.g., biological, magnetic recording, etc.) where both ferromagnetism and tribological/adhesion properties act synergistically to optimize material performance.

Sub-micron magnetic patterns and local variations of adhesion force induced in non-ferromagnetic amorphous steel by femtosecond pulsed laser irradiation

Huiyan Zhang[a], Yuping Feng[a], Daniel Nieto[b], Eva García-Lecina[c], Clare Mcdaniel[d], Jordi Díaz-Marcos[e], María Teresa Flores-Arias[b], Gerard M O'connor[d], Maria Dolors Baró[a], Eva Pellicer[a,*] and Jordi Sort[f,§]

[a]Departament de Física, Universitat Autònoma de Barcelona, E08193 Bellaterra, Spain.

[b]Microoptics and GRIN Optics Group, Applied Physics Department, University of Santiago de Compostela, E15782 Santiago de Compostela, Spain.

[c]Unidad de Superficies Metálicas, IK4-CIDETEC, E20009 Donostia-San Sebastián (Gipuzkoa), Spain.

[d]National Centre for Laser Applications, School of Physics, National University of Ireland, Galway, Ireland.

[e]Unitat de Tècniques Nanomètriques, Centres Científics i Tecnològics, Universitat de Barcelona, E08028 Barcelona, Spain.

[f]Institució Catalana de Recerca i Estudis Avançats (ICREA) and Departament de Física, Universitat Autònoma de Barcelona, E08193 Bellaterra, Spain.

To whom correspondence should be addressed: *eva.pellicer@uab.cat; §jordi.sort@uab.cat

Applied Surface Science 371 (2016) 399–406

Contents lists available at ScienceDirect

Applied Surface Science

journal homepage: www.elsevier.com/locate/apsusc

Sub-micron magnetic patterns and local variations of adhesion force induced in non-ferromagnetic amorphous steel by femtosecond pulsed laser irradiation

Huiyan Zhang[a], Yuping Feng[a], Daniel Nieto[b], Eva García-Lecina[c], Clare Mcdaniel[d], Jordi Díaz-Marcos[e], María Teresa Flores-Arias[b], Gerard M. O'connor[d], Maria Dolors Baró[a], Eva Pellicer[a,*], Jordi Sort[f,*]

[a] *Departament de Física, Universitat Autònoma de Barcelona, Bellaterra, E08193, Spain*
[b] *Microoptics and GRIN Optics Group, Applied Physics Department, University of Santiago de Compostela, E15782 Santiago de Compostela, Spain*
[c] *Unidad de Superficies Metálicas, IK4-CIDETEC, E20009 Donostia-San Sebastián Gipuzkoa, Spain*
[d] *National Centre for Laser Applications, School of Physics, National University of Ireland, Galway, Ireland*
[e] *Unitat de Tècniques Nanomètriques, Centres Científics i Tecnològics, Universitat de Barcelona, E08028 Barcelona, Spain*
[f] *Institució Catalana de Recerca i Estudis Avançats (ICREA) and Departament de Física, Universitat Autònoma de Barcelona, Bellaterra, E08193, Spain*

ARTICLE INFO

Article history:
Received 16 October 2015
Received in revised form 29 February 2016
Accepted 1 March 2016
Available online 3 March 2016

Keywords:
Femtosecond pulsed laser irradiation
Amorphous steel
Magnetic patterning
Surface ripples
Adhesion force
Wettability

ABSTRACT

Periodic ripple and nanoripple patterns are formed at the surface of amorphous steel after femtosecond pulsed laser irradiation (FSPLI). Formation of such ripples is accompanied with the emergence of a surface ferromagnetic behavior which is not initially present in the non-irradiated amorphous steel. The occurrence of ferromagnetic properties is associated with the laser-induced devitrification of the glassy structure to form ferromagnetic (α-Fe and Fe_3C) and ferrimagnetic [$(Fe,Mn)_3O_4$ and Fe_2CrO_4] phases located in the ripples. The generation of magnetic structures by FSPLI turns out to be one of the fastest ways to induce magnetic patterning without the need of any shadow mask. Furthermore, local variations of the adhesion force, wettability and nanomechanical properties are also observed and compared to those of the as-cast amorphous alloy. These effects are of interest for applications (e.g., biological, magnetic recording, etc.) where both ferromagnetism and tribological/adhesion properties act synergistically to optimize material performance.

1. Introduction

The unprecedented technological progress in diverse areas of nanoscience and nanotechnology is raising an increasing demand for new types of materials, novel lithographic procedures and new techniques to assemble micro-/nanocomponents into complex systems, such as micro-/nanodevices, lab-on-a-chip or miniaturized robotic platforms. To a large extent, coping with the current technological challenges relies on the implementation of innovative methods to fabricate large areas of patterned structures with sub-micrometer scale precision in a rapid, inexpensive and industrially scalable manner.

High-resolution magnetic patterning is crucial in applications like magnetic encoding, magnetic sensors and actuators, wirelessly actuated magnetic microrobots, spin-electronics or high-density magnetic recording media. In all these applications, not only the magnetic properties are important but other aspects, such as surface adhesion, nanomechanical behavior or hydrophobicity need to be precisely controlled in order to attain optimized material performance. The tribological behavior of patterned magnetic materials and the quantification of surface adhesion forces, for example, are of paramount importance in high-density recording media, where the write/read heads fly only a few nm from the surface of the recorded information [1]. Adhesion is a crucial parameter in magnetic systems for biological and mechatronic applications [2,3], in some bioinspired actuator devices [4] or in magnetic wall-climbing devices [5]. Surface roughness plays also a crucial role on the magneto-electrical properties of a variety of thin films [6,7].

In many of these cases it is desirable that the magnetic behavior of the patterned structures is not affected by the presence of magnetic stray fields stemming from neighboring magnetic materials or underlying magnetic layers. For this reason, sophisticated lithographic procedures, that are usually rather time-consuming (i.e., consisting of multiple steps) and rather costly (i.e., requiring

---

* Corresponding authors.
E-mail addresses: eva.pellicer@uab.cat (E. Pellicer), jordi.sort@uab.cat (J. Sort).

http://dx.doi.org/10.1016/j.apsusc.2016.03.011
0169-4332/

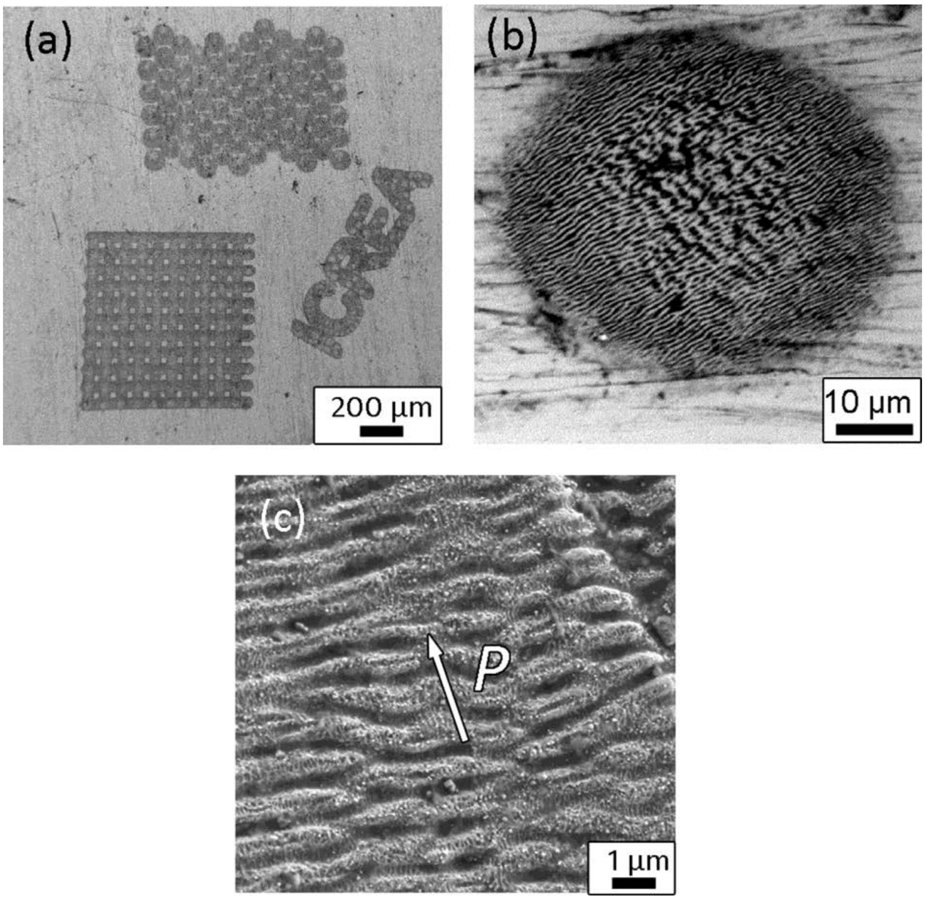

Fig. 1. (a) SEM images (secondary electrons) of different patterns written at the surface of the $Fe_{51}Mn_{10}Cr_4Mo_{12}C_{15}B_6Er_2$ alloy by femtosecond pulsed laser irradiation (FSPLI) with 95% overlapped 500 fs laser pulses and applied fluence 0.33 J/cm^2; (b) detail of a circular dot obtained by FSPLI imaged by SEM; (c) magnified SEM view of the so-called "classical ripples" formed during the FSPLI process, whose direction is perpendicular to the polarization of the incident laser (*P*).

clean room facilities), are utilized to fabricate arrays of ferromagnetic dots at the surface of non-ferromagnetic substrates [8].

In the last few years, some non-conventional approaches for the direct magnetic patterning of initially non-magnetic materials have been developed. These include, for example, nanoindentation and ion irradiation of atomically-ordered alloys, stainless steels or metallic glasses [9–13]. The large compressive stresses generated during nanoindentation are sufficient to induce atomic order-disorder transitions in Fe-Al alloys, local nanocrystallization in metallic glasses or martensitic transformations in austenitic steels. In all these cases, the induced structural changes result in localized magnetic patterning at specific regions of the sample surface [9–11]. Ion irradiation through shadow masks is an alternative procedure to fabricate arrays of ferromagnetic structures (sometimes without any topological damage) in some of the aforementioned materials [12,13].

Femtosecond pulsed laser irradiation (FSPLI) is a powerful technique to induce periodic topological patterning and concomitant ablation damage at the surface of certain metallic alloys, semiconductors, dielectrics and polymers [14–24]. Depending on the laser processing conditions (fluence and nominal number of pulses) the imprinted structures can change from low-spatial-frequency ripples or "classical ripples" with periodicity close to the laser light (perpendicular to the polarization of the incident laser beam) [16,17] to high-spatial-frequency nanoripples with periodicity smaller than laser wavelength (either perpendicular or parallel to the polarization direction [17–19]. Even spikes [20], regular arrays of nanopores [21] or concentric rings [22] can be induced under certain circumstances. Several models have been put forward in the literature to account for the various types of ripple topologies. Examples include the interference between the laser beam and the surface scattered wave, the excitation of surface plasmon polaritons, and self-organization. Regarding interference, it is proposed that when a laser beam interacts with a material, surface defects cause the incoming incident laser beam to become partially scattered into a tangential wave, which propagates across the material surface. Laser-induced periodic surface structures are thought to appear because of interference of the laser beam scattered by multiple surface defects [23]. Separately, it has been reported that when the incident electromagnetic laser radiation couples with a plasmon charge oscillation, a modified electromagnetic field propagates in the area which has specific polarization dependence, regardless of whether a material is metallic or dielectric in nature [24–26]. For metals, a specific dependence of the plasmon coupling has been reported depending on the grating period [27]. Furthermore, ripple formation has been compared to the formation of sand dunes present in a desert and to other structures spontaneously created following ion beam sputtering on a microscale [28]. These spontaneous processes include the melting and resolidification processes occurring at the surface due to the induced temperature gradients [29–31]. Additionally, second harmonic generation has been shown to play a role in the formation of nanoripples [32]. In spite of the very short duration of the pulses, phase transformations and other microstructural changes are sometimes observed during FSPLI, for example amorphization of Si [15], crystallization of chalcogenides [33] or crystallization of metallic glasses [31,34].

In addition to its fundamental interest, surface treatment using FSPLI is also appealing for practical applications, as a method to increase the corrosion resistance of steel [35], to induce superhydrophobicity in several alloys [36] or to improve the bending plasticity in certain types of metallic glasses [37]. Remarkably, most of previous works dealing with FSPLI have focused on the mechanisms responsible for topological surface corrugation or on the variation of macroscopic physico-chemical properties at the surface level treating the material as a whole [18,19,38–42]. Conversely, detailed mappings of physical properties at the micro-/nanoscale (i.e., at the “ripples” length-scales) have been mainly overlooked. In particular, the use of FSPLI as a method to induce magnetic patterning has not been demonstrated.

In this work, we report on the utilization of FSPLI to induce magnetic patterning at the surface of $Fe_{51}Mn_{10}Cr_4Mo_{12}C_{15}B_6Er_2$ alloy. Fe(Co)–Cr–Mo–C–B–Ln and Fe–Cr–Mn–Mo–C–B–Ln (where Ln=lanthanide element) alloys, with Fe(Co) content around 50 at.%, have been intensively investigated during the last few years owing to their high glass forming ability, outstanding mechanical properties and high corrosion resistance [43,44]. For certain compositional ranges, the presence of small metalloid atoms (C, B) together with large refractory metals (Cr, Mo) promotes the formation of a glassy microstructure which does not exhibit long-range crystallographic order. In these alloys, Mn is known to play a crucial role in increasing the reduced glass transition temperature [45], while suppressing the ferromagnetic behavior at room temperature. These materials, often referred to as “non-ferromagnetic amorphous alloys”, exhibit a yield stress that can be about three times larger than that of crystalline austenitic stainless steel. The alloy composition chosen in our study corresponds to the one that exhibits the largest glass forming ability among the Fe–Cr–Mo–C–B–Ln alloy system [46]. A self-induced mechanism leading to the formation of periodic microstructures has been observed during femtosecond pulsed laser ablation at the surface of this material. Besides the formation of low-spatial-frequency ferromagnetic ridges perpendicular to the polarization of the incident laser beam, high-spatial-frequency nanoripples (parallel to the laser polarization) are also formed between consecutive low-frequency ridges. The observed ferromagnetic behavior is ascribed to surface-crystallization of some ferromagnetic (α-Fe, Fe_3C) or ferrimagnetic [like $(Fe,Mn)_3O_4$ or Fe_2CrO_4] phases during the FSPLI process. These results show a potentially new application of FSPLI, as a tool to magnetically pattern large areas (~cm^2) of a non-magnetic material in a very fast (few seconds) and inexpensive manner. Furthermore, a mapping of the local variation of nano-mechanical properties (adhesion force) at the FSPLI treated surface was obtained by atomic force microscopy (AFM) with Peak Force tapping mode.

2. Experimental procedure

The $Fe_{51}Mn_{10}Cr_4Mo_{12}C_{15}B_6Er_2$ alloy was prepared by arc-melting a mixture of the high purity elements (99.9 wt.%) under a Ti-gettered Ar atmosphere. The master alloy was then injected into a copper mold to produce cylindrical rods with a diameter of 5 mm. The rods were subsequently cut into discs with a thickness of 2 mm and polished using diamond paste. The FSPLI treatment was performed in air (ambient conditions) using s-Pulse HP (Amplitude Systemes) comprising a Diode Pumped Femtosecond laser based on Ytterbium crystal technology. The incident direction of the laser was orthogonal to the sample plane. The irradiation conditions were: applied fluence of 0.33 J/cm^2, laser spot of 20 μm, wavelength of 1030 nm, repetition rate of 100 kHz, pulse-width of 500 fs and sample scan speed of 200 mm/s; 50 passes of highly overlapped (95%) pulses were used. Large areas (of 3 × 3 mm^2) as well as arrays of squares, circles and lines (with widths down to 20 μm) were prepared using the same irradiation conditions. Note that, contrary to other studies where the sample is irradiated *N* times at each given location, in our case the sample was kept in motion during the surface treatment and a strong pulse overlapping was employed. This method is very effective in accelerating the processing times while the obtained results are similar to conventional pulsed laser treatments. For instance, an area of 1 cm^2 can be processed in about only 10 s. Structural characterization of the as-cast and laser treated samples was carried out by x-ray diffraction (XRD) using Cu Kα radiation (Philips X'Pert diffractometer). The surface morphology was investigated by two separate AFMs, i.e., an Agilent 5500 and a Multimode 8 with Nanoscope electronics V from Bruker. Both the surface roughness and adhesion were evaluated, the latter using the Peak Force tapping QNM mode from Bruker. Detailed observations of the ripples were performed by means of field-emission scanning electron microscopy (FESEM, Zeiss Merlin), coupled with energy-dispersive X-ray (EDX) for compositional analyses. Magnetization versus applied field curves were recorded at room temperature by means of a vibrating sample magnetometer (VSM) from Oxford Instruments. The generated ferromagnetic patterns were observed by magnetic force microscopy (MFM) at a lift height of 100 nm using a setup from Danish Microengineering and Si tips coated with CoCr alloy. Nanoindentation experiments were performed using a UMIS indenter from Fischer Cripps Laboratories, with a Berkovich-type pyramidal-shaped diamond tip, in load control mode, applying a maximum load of 10 mN. The hardness and reduced Young's modulus were calculated from the unloading indentation segments, using the method of Oliver and Pharr [47]. Finally, contact-angle measurements were performed using the sessile-drop technique (5 wt.% NaCl aqueous solution droplets with 1 μL volume).

3. Results and discussion

Fig. 1 (a) shows some examples of the patterns that can be induced by FSPLI imaged by SEM. Honeycomb arrays of circular dots, digits and letters and networks of stripes can be drawn at the surface of the metallic glass in a very fast way (few seconds), with a precision determined by the laser spot (in this case 20 μm). The processing times are orders of magnitude faster than those involved in multi-step conventional patterning methods such as optical or electron beam lithography. The lateral resolution of the areas printed by FSPLI is comparable to the one attained with other direct patterning techniques, such as inkjet printing technology (typically of several tens of μm), that still requires, in any case, of shadow masks [48].

Fig. 1 (b) reveals that surface corrugation occurs at the micrometer length scale inside each laser irradiated spot. Periodic arrays of ripples, oriented perpendicular to the laser polarization (*P*), are formed spontaneously [Fig. 1 (c)]. The periodicity of these “classical ripples” is 770 ± 28 nm, hence slightly smaller than the wavelength of the laser, in agreement with other works from the literature [18,20,21,32]. The depth of the ridges is 238 ± 9 nm (Fig. 2 (a) and (b)). The magnified views of the classical ripples at the FSPLI treated surfaces, with and without vertically tilting the sample plane by 45° with respect to the x-y plane are shown in Fig. 3. Remarkably, abundant nanoripples are observed between consecutive ridges by the high-resolution SEM. The orientation of the nanoripples is perpendicular to the classical ripples (i.e., parallel to the polarization of the incident laser). The nanoripples exhibit average width of ~100–300 nm [Fig. 3 (a)] and thickness of few tens of nm (Fig. 3 (b)). The formation of nanoripples between classical ripples has been previously reported according to the sur-

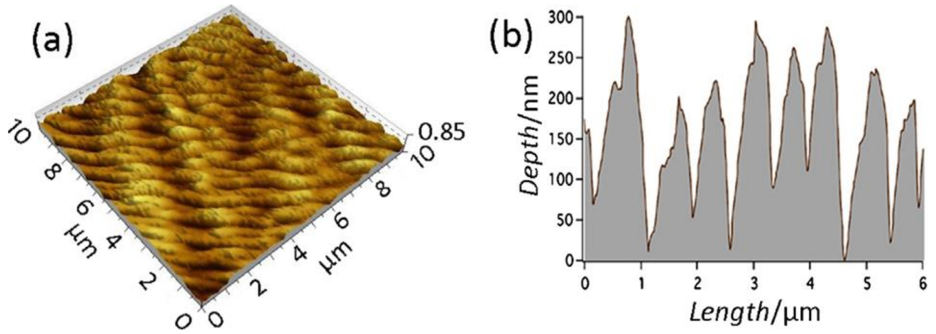

Fig. 2. (a) AFM image of the classical ripples; (b) representative AFM line profile measured along the direction orthogonal to the ripples long axis.

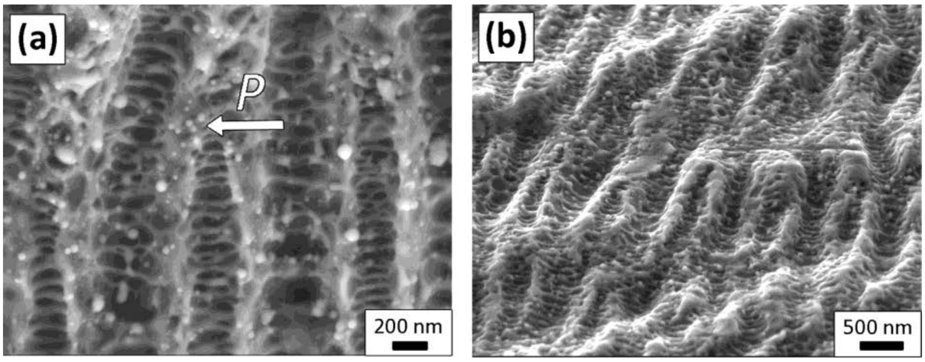

Fig. 3. High-resolution SEM images of the classical ripples at the FSPLI treated surfaces (a) without and (b) with vertically tilting the sample plane by 45° with respect to the x-y plane, respectively, showing the presence (and the depth) of "nanoripples" at the trenches between consecutive ridges, with orientation parallel to the polarization direction of the incident laser beam (P).

face plasmon interference model combined with grating-assisted coupling. The high-spatial-frequency nanoripples are formed as common walls between adjacent bursting bubbles, while low-spatial-frequency classical ripples are then formed as hills between individual expanding events [18]. The ripple formation observed in this study is consistent with the coupling of the incident electromagnetic radiation with plasmon charge oscillations. It can be proposed that the roughness of the initial surface is sufficient to initiate this plasmon polariton coupling. When overlapped pulses are used, the nano- structures/ripples created from preceding pulses, will also lead to such coupled surface excitations. The coupled plasmon polariton modes in turn decay non-radiatively and thereby create a unique spatial energy distribution across the surface. Using recently reported results [49] it can be speculated that this distribution leads to the bifuricated and bended ripple structure observed throughout Figs. 1, 2 and 3.

The XRD patterns of the as-cast $Fe_{51}Mn_{10}Cr_4Mo_{12}C_{15}B_6Er_2$ alloy and the FSPLI treated ($3 \times 3\,mm^2$) sample are shown in Fig. 4. The diffractogram of the as-cast sample consists of two broad halos with virtually no sharp peaks superimposed. This indicates that the as-cast rod is mainly amorphous. Conversely, clear diffraction peaks are observed in the XRD pattern of the pulsed laser treated sample. Both metallic and oxide phases are generated during FSPLI. Crystallization is expected because, in spite of the short duration of the pulses, temperature is often estimated to locally reach thousands of K in this type of processes [29,50], thus much higher than the glass transition, crystallization and even liquidus temperatures of the $Fe_{51}Mn_{10}Cr_4Mo_{12}C_{15}B_6Er_2$ alloy [46].

It is remarkable that some of the crystallized phases are ferromagnetic at room temperature (α-Fe and Fe_3C exhibit Curie temperatures, T_C, of 1044 K and 480 K, respectively) [51], whereas $(Fe,Mn)_3O_4$ and Fe_2CrO_4 are both ferrimagnetic ($T_{C,(Fe,Mn)3O4} > 570\,K$ [52], $T_{C,Fe2CrO4} = 553\,K$ [53]). Other phases (e.g., C_2CrO_4 or MoB_2 are neither ferromagnetic nor ferrimagnetic). In Fig. 5, EDX mappings reveal that the ridges are enriched in Fe, Mn, Cr and O. Although the ripples structure is also observed in the C mapping, the zones enriched in C do not always exactly coincide with the ridges topology. In turn, Mo and Er are homogeneously distributed at the surface. These results indicate that the ferromagnetic/ferrimagnetic phases are mainly located at the ripples of the FSPLI regions. The deposited energy, delivered in this multipulse approach, appears sufficient to establish a temperature which enables redistribution of the atomic species. However, the precise mechanism for this effect is not clear, and hence it must be interpreted with caution.

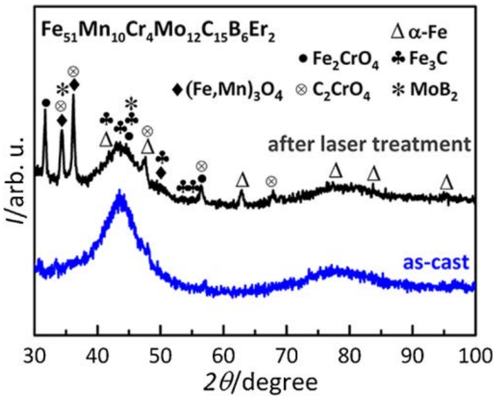

Fig. 4. X-ray diffraction patterns corresponding to the as-cast glassy alloy and the FSPLI surface-treated alloy.

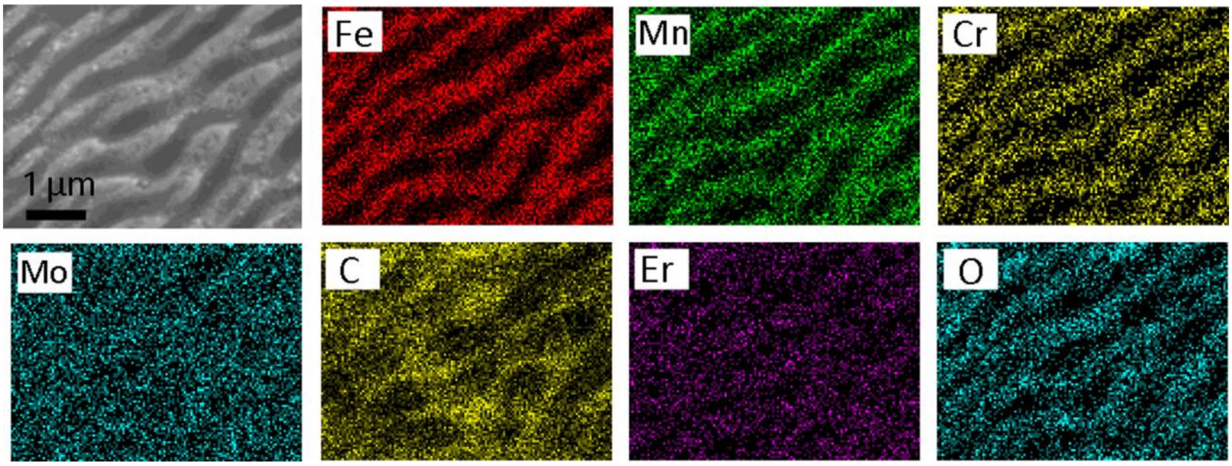

Fig. 5. Secondary-electrons SEM image of the classical ripples, together with the corresponding elemental mappings (Fe, Mn, Cr, Mo, C, Er and O), as obtained from energy-dispersive X-ray (EDX) analyses.

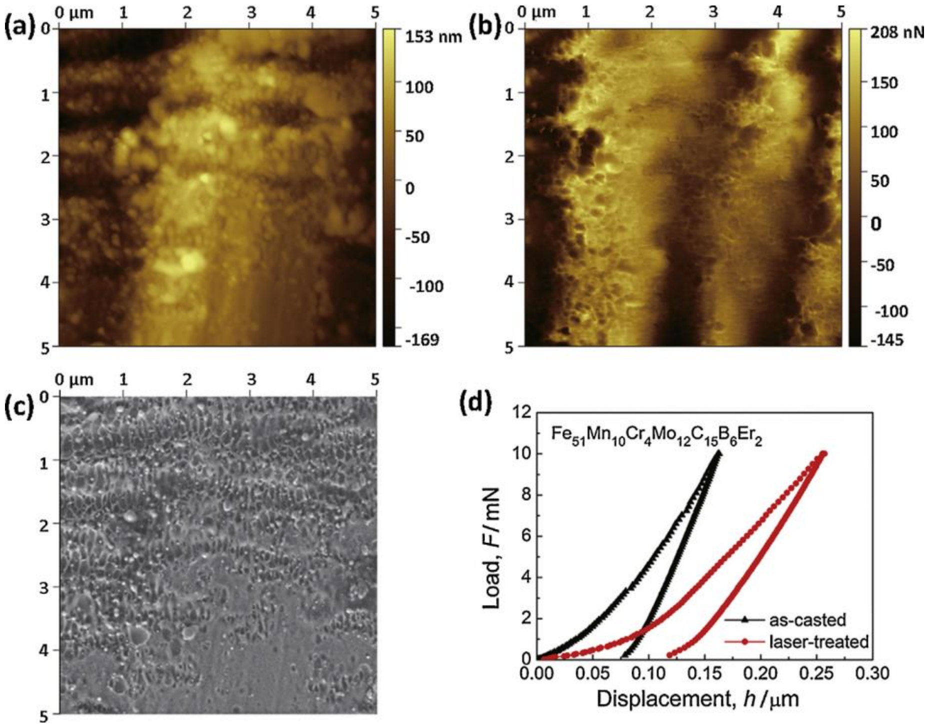

Fig. 6. Images of FSPLI treated sample (corresponding to the circular pattern in Fig. 1(a)): (a) topography and (b) adhesion force of the FSPLI treated surface, both obtained by AFM. For comparison, (c) is an SEM image of the same area as the AFM images. (d) Representative load (F)-displacement (h) nanoindentation curves corresponding to the as-cast and FSPLI treated samples.

Interestingly, the nanoripples can also be observed by AFM, not only when using the conventional topographic tapping mode (Fig. 6(a)) but particularly when the system is operated in the "Peak Force Quantitative Nanomechanical mode" (QNM mode) (Fig. 6 (b)). For comparison, the SEM image of the same area is displayed in Fig. 6 (c). Under certain conditions, this QNM method allows extracting the mechanical properties of the scanned surface with sub-micrometer scale resolution. In peak-force tapping mode, the tip and the sample are intermittently brought into contact. However, the sample deformation depths are limited to a few nanometers and, therefore, only the elastic regime is actually probed. At such small applied force range, adhesion forces between the sample and the tip play an important role and they can be quantified. The adhesion mapping reveals maximum adhesion at the upper parts of the ripples and minimum contrast at the trenches. To our knowledge, this local variation of adhesion behavior after FSPLI has not been previously reported in the literature. Variations in adhesion of the order of hundreds of nN were observed between the different regions comprising the nanoripples [Fig. 6 (b)]. Interestingly, the average adhesion value in the FSPLI sample ($<F_{adh}> \sim 190$ nN) is considerably higher than for the as-cast alloy (where the mean adhesion force is only around 30 nN), in agreement with previous results showing that an increase of surface roughness induces higher adhesion force in the material as a whole [42]. For soft materials (e.g., polymers) also the Young's modulus can be determined by AFM using the QNM operation mode [54].

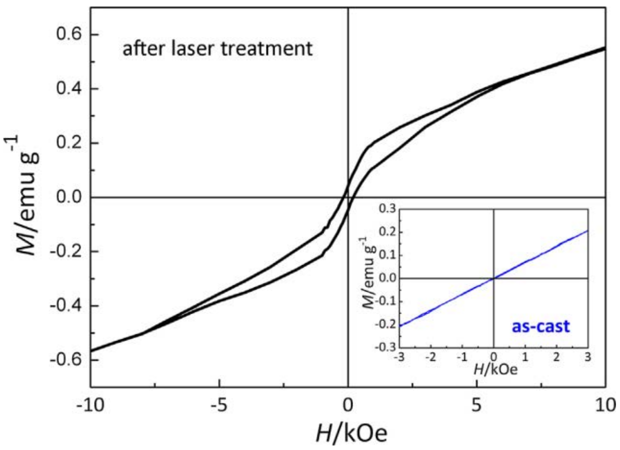

Fig. 7. Hysteresis loop corresponding to the $Fe_{51}Mn_{10}Cr_4Mo_{12}C_{15}B_6Er_2$ alloy after FSPLI treatment, applying the magnetic field parallel to the ripples direction. The inset shows the dependence of the magnetization (M) as a function of applied magnetic field (H) for the as-cast $Fe_{51}Mn_{10}Cr_4Mo_{12}C_{15}B_6Er_2$ alloy, which is paramagnetic.

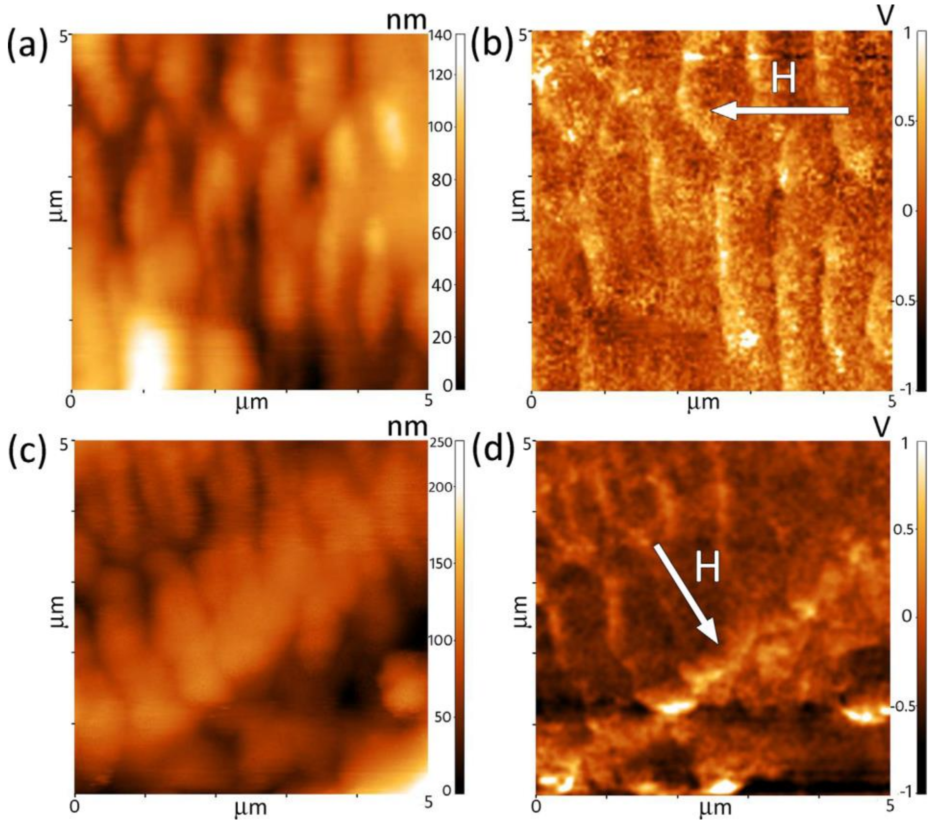

Fig. 8. (a,c) representative AFM images of the classical ripples together with (b,d) the corresponding MFM images obtained at remanence after having saturated the sample with a strong magnetic field (H = 5000 Oe) along the directions perpendicular and parallel to the ripples long axis (as indicated by the white arrows), respectively.

However, for hard materials (like the one studied in this work), the quantification of Young's modulus using the QNM mode becomes rather unreliable. Thus, nanoindentation was employed to evaluate the Berkovich hardness, H_B, and reduced Young's modulus (E_r) of the as-cast and laser treated samples. As shown in Fig. 6 (d), for a maximum load of 10 mN, higher penetration depth is attained in the laser treated sample, indicating that FSPLI induces mechanical softening at the surface. The hardness decreases from H_B = 14 GPa to H_B = 9.5 GPa after FSPLI. Similarly, E_r decreases from 193 to 83 GPa. Such variations of surface mechanical properties can be ascribed to the increase of surface roughness caused by the laser irradiation [55,56]. The occurrence of roughness and surface corrugation is known to also play a crucial role in the hydrophobicity properties of surfaces. Here an increase of contact angle, from 64° to 75° is observed after FSPLI. This increase is quite modest compared to the results obtained from other rougher surfaces prepared by different methods. Namely, certain FSPLI conditions can render superhydrophobic surfaces by adjusting both the topological damage as well as the composition of the alloy at surface level [36].

Shown in Fig. 7 is the hysteresis loop of the $Fe_{51}Mn_{10}Cr_4Mo_{12}C_{15}B_6Er_2$ alloy after FSPLI surface treatment, recorded along the ripples direction. The clear ferromagnetic response is in contrast to the paramagnetic behavior of the as-cast alloy, as shown in the inset. Actually, more than one ferromagnetic-like contribution are visible in the hysteresis loop of the laser-treated sample, suggesting the co-existence of phases with lower coercivity (presumably due to the soft-magnetic α-Fe and Fe_3C phases) with others magnetically harder (such as the semi-hard ferrimagnetic $(Fe,Mn)_3O_4$ or Fe_2CrO_4 phases). Comparative AFM/MFM mappings of the classical ripples generated at the surface of the amorphous steel after FSPLI are shown in Fig. 8. The MFM images were acquired at the remanent state after applying a magnetic field (H = 5000 Oe) either parallel or perpendicular to the long axis of the ripples. In spite of the obvious analogies between the AFM (topological) and MFM (magnetic) images [cf. panels (a) and (c) with panels (b) and (d)], it is clear that the two types of mappings do not match each other, evidencing that the MFM contrast is not merely due to topological surface variations. Namely, dark and bright areas are observed inside each ripple in the MFM images, indicating a clear magnetic dipolar contrast. As expected, the orientation of such dipolar contrast depends on the direction of the previously applied magnetic field. Although the as-cast $Fe_{51}Mn_{10}Cr_4Mo_{12}C_{15}B_6Er_2$ alloy is paramagnetic, the magnetic contrast observed by MFM can be actually expected, given the ferro-/ferrimagnetic nature of the crystalline phases formed during the laser treatment at the alloy surface.

It should be noted that the magnetic patterning induced by FSPLI is accompanied with topological patterning and is irreversible in nature (i.e., it remains at the surface unless the sample is mechanically polished to remove the ripples). This is opposite to the ion-irradiation induced magnetic patterning in $Fe_{60}Al_{40}$ alloy [13], which preserved the smoothness of the surface and could be erased by subsequent low-temperature annealing treatments. In that case, however, a pre-lithographed mask was needed to define the local regions through which the ions could irradiate the atomically-ordered alloy, whereas FSPLI is completely mask-free. Hence, compared to ion-irradiation, FSPLI is a single-step magnetic patterning method and a cost-effective lithographic procedure. As aforementioned, nanoindentation can also generate arrays of ferromagnetic dots at the surface of various alloys, including metallic glasses. However, compared to FSPLI, nanoindentation is very slow. About one or two minutes are needed to make each indentation impression and induce the concomitant magnetic patterning. Hence, an array of 10 × 10 indentations covering an area of 1 cm^2 would take about 2–3 h. Conversely, inducing magnetic patterning in this 1 cm^2 region by FSPLI needs only about 10 s. Thus, the FSPLI is much faster. Given the inherent topological patterning that accompanies FSPLI treatments, the induced magnetic structures could be used for applications like magnetic traps (of, for example, magnetic nanoparticles dispersed in fluids), magnetic sensors or magnetic encoders.

4. Conclusion

In summary, FSPLI has been shown to be a suitable method to generate periodic arrays of sub-micrometer-sized magnetic structures at the surface of non-ferromagnetic amorphous steel. The origin of the observed ferromagnetic behavior is the laser-induced devitrification of the glassy structure to form ferromagnetic (α-Fe and Fe_3C) and ferrimagnetic [$(Fe,Mn)_3O_4$ and Fe_2CrO_4] phases. Besides the formation of ferromagnetic low-spatial-frequency ripples, much smaller nanoripples (of a few tens of nm in lateral size) are also generated during the FSPLI process, which is consistent with the coupling of the incident electromagnetic radiation with plasmon charge oscillations. Such nanoripples are clearly observed by high-resolution SEM and AFM and give rise to local variations of the adhesion force during AFM scanning. The observed variations in adhesion force can be particularly important for certain applications like traps for magnetic nanoparticles, where an exceedingly hydrophobic surface would not be desirable. The wettability and nanomechanical properties of the FSPLI have been also studied and compared to those of the as-cast amorphous alloy. The generation of magnetic structures by FSPLI turns out to be one of the fastest ways to induce magnetic patterning without the need of any shadow mask. The magnetic patterning procedure reported in this work can also be extrapolated to other materials, such as non-ferromagnetic intermetallic alloys, austenitic steel or other types of non-magnetic metallic glasses, although the origin of the induced ferromagnetism could vary depending on the system under investigation.

Acknowledgements

This work has been partially funded by the 2014-SGR-1015 project from the *Generalitat de Catalunya* and the MAT2014-57960-C3-1-R (co-financed by the *Fondo Europeo de Desarrollo Regional*, FEDER) and MAT2014-57960-C3-2-R from the Spanish *Ministerio de Economía y Competitividad* (MINECO). Partial funding from the *Consellería de Cultura, Xunta de Galicia*, Spain, under the contract EM2012/019, is also acknowledged. Dr. Eva Pellicer is grateful to MINECO for the “Ramon y Cajal” contract (RYC-2012-10839).

References

[1] S.-C. Lee, A.A. Polycarpou, Adhesion forces for sub-10 nm flying-height magnetic storage head disk interfaces, ASME J. Tribol. 126 (2004) 334–341.
[2] V. Iacovacci, L. Ricotti, P. Dario, A. Menciassi, Design and development of a mechatronic system for noninvasive refilling of implantable artificial pancreas, IEEE/ASME Trans. Mechatron. 20 (2014) 1160–1169.
[3] M. Dkhil, A. Bolopion, S. Régnier, M. Gauthier, Optimization of the size of a magnetic microrobot for high throughput handling of micro-objects, IEEE/ASME Int. Conf. AIM (2014) 372–377.
[4] D.M. Drotlef, P. Blümler, A. del Campo, Magnetically actuated patterns for bioinspired reversible adhesion (dry and wet), Adv. Mater. 26 (2014) 775–779.
[5] N.R. Khirad, R.K. Sanghi, D.J. Tidke, Magnetic wall climbing devices—a review, IOSR J. Mech. Civil Eng. 7 (2014) 55–59.
[6] G. Palasantzas, J.T.M. De Hosson, J. Barnas, Surface/interface roughness effects on magneto-electrical properties of thin films, Surf. Sci. 507-510 (2002) 541–545.
[7] Y.P. Zhao, R.M. Gamache, G.C. Wang, T.M. Lu, G. Palasantzas, J.T.M. De Hosson, Effect of surface roughness on magnetic domain wall thickness domain size, and coercivity, J. Appl. Phys. 89 (2001) 1325–1330.
[8] J.I. Martín, J. Nogués, K. Liu, J.L. Vicent, I.K. Schuller, Ordered magnetic nanostructures: fabrication and properties, J. Magn. Magn. Mater. 256 (2003) 449–501.
[9] J. Sort, A. Concustell, E. Menéndez, S. Suriñach, M.D. Baró, J. Farran, J. Nogués, Selective generation of local ferromagnetism in austenitic stainless steel using nanoindentation, Appl. Phys. Lett. 89 (2006) 032509.
[10] J. Sort, A. Concustell, E. Menéndez, S. Suriñach, K.V. Rao, S.C. Deevi, M. D. Baró, J. Nogués, Periodic arrays of micrometer and sub-micrometer magnetic structures prepared by nanoindentation of a nonmagnetic intermetallic compound, Adv. Mater. 18 (2006) 1717–1720.
[11] J. Sort, L.F. Bonavina, A. Varea, C. Souza, W.J. Botta, C.S. Kiminami, C. Bolfarini, S. Suriñach, M.D. Baró, J. Nogués, Out-of-plane magnetic patterning based on indentation-induced nanocrystallization of a metallic glass, Small 6 (2010) 1543–1549.
[12] R. Bali, S. Wintz, F. Meutzner, R. Hübner, R. Boucher, A.A. Ünal, S. Valencia, A. Neudert, K. Potzger, J. Bauch, F. Kronast, S. Facsko, J. Lindner, J. Fassbender, Printing nearly-discrete magnetic patterns using chemical disorder induced ferromagnetism, Nano Lett. 14 (2014) 435–441.
[13] E. Menéndez, M.O. Liedke, J. Fassbender, T. Gemming, A. Weber, L.J. Heyderman, K.V. Rao, S.C. Deevi, S. Suriñach, M.D. Baró, J. Sort, J. Nogués, Direct magnetic patterning due to the generation of ferromagnetism by selective ion irradiation of paramagnetic FeAl alloys, Small 5 (2009) 229–234.
[14] C. De Marco, S.M. Eaton, R. Suriano, S. Turri, M. Levi, R. Ramponi, G. Cerullo, R. Osellame, Surface properties of femtosecond laser ablated PMMA, ACS Appl. Mater. Interfaces 2 (2010) 2377–2384.
[15] J. Jia, M. Li, C.V. Thompson, Amorphization of silicon by femtosecond laser pulses, Appl. Phys. Lett. 84 (2004) 3205–3207.
[16] L.L. Ran, S.L. Qu, Structure formation on the surface of alloys irradiated by femtosecond laser pulses, Appl. Surf. Sci. 256 (2010) 2315–2318.
[17] N. Yasumaru, E. Sentoku, K. Miyazaki, J. Kiuchi, Femtosecond-laser-induced nanostructure formed on nitrided stainless steel, Appl. Surf. Sci. 264 (2013) 611–615.

[18] J. Vincenc Obona, V. Ocelík, J.Z.P. Skolski, V.S. Mitko, G.R.B.E. Römer, A.J. Huis in't Veld, J.T.M. De Hosson, On the surface topography of ultrashort laser pulse treated steel surfaces, Appl. Surf. Sci. 258 (2011) 1555–1560.

[19] J.Z.P. Skolski, G.R.B.E. Römer, J.V. Obona, V. Ocelik, A.J. Huis In't Veld, J.T.M. De Hosson, Laser-induced periodic surface structures: fingerprints of light localization, Rev. Phys. B Condens. Matter Mater. Phys. 85 (2012) 1–9.

[20] W. Zhang, G.H. Cheng, Q. Feng, L.M. Cao, Picosecond laser-induced formation of spikes in a single crystal superalloy, Appl. Surf. Sci. 258 (2012) 9452–9456.

[21] W. Zhang, G. Cheng, X.D. Hui, Q. Feng, Abnormal ripple patterns with enhanced regularity and continuity in a bulk metallic glass induced by femtosecond laser irradiation, Appl. Phys. A 115 (2014) 1451–1455.

[22] F.X. Ma, J.J. Yang, X.N. Zhu, C.Y. Liang, H.S. Wang, Femtosecond laser-induced concentric ring microstructures on Zr-based metallic glass, Appl. Surf. Sci. 256 (2010) 3653–3660.

[23] A.E. Siegman, P.M. Fauchet, Stimulated Wood's anomalies on laser-illuminated surfaces, IEEE J. Quantum Electron. 22 (1986) 1384–1403.

[24] M. Huang, F.L. Zhao, Y. Cheng, N.S. Xu, Z.Z. Xu, Origin of laser-induced near-subwavelength ripples: interference between surface plasmons and incident laser, ACS Nano 3 (2009) 4062–4070.

[25] T.J.Y. Derrien, R. Koter, J. Crüger, S. Höhm, A. Rosenfeld, J. Bonse, Plasmonic formation mechanism of periodic 100-nm-structures upon femtosecond laser irradiation of silicon in water, J. Appl. Phys. 116 (2014) 074902.

[26] J.C. Wang, C.L. Guo, Ultrafast dynamics of femtosecond laser-induced periodic surface pattern formation on metals, Appl. Phys. Lett. 87 (2005) 251914.

[27] F. Garrelie, J. Colombier, F. Pigeon, S. Tonchev, N. Faure, M. Bounhalli, S. Reynaud, O. Parriaux, Evidence of surface plasmon resonance in ultrafast laser-induced ripples, Opt. Express 19 (2011) 9035–9043.

[28] J. Reif, O. Varlamova, F. Costache, Femtosecond laser induced nanostructure formation: self-organization control parameters, Appl. Phys. A: Mater. Sci. Process. 92 (2008) 1019–1024.

[29] L.V. Zhigilei, Z.B. Lin, D.S. Ivanov, Atomistic modeling of short pulse laser ablation of metals: connections between melting, spallation, and phase explosion, J. Phys. Chem. C 113 (2009) 11892–11906.

[30] E. Bévillon, J.P. Colombier, B. Dutta, R. Stoian, Ab initio nonequilibrium thermodynamic and transport properties of ultrafast laser irradiated 316L stainless steel, J. Phys. Chem. C 119 (2015) 11438–11446.

[31] Y. Zhang, L. Liu, G. Zou, N. Chen, A. Wu, H. Bai, Y. Zhou, Femtosecond laser-induced phase transformations in amorphous $Cu_{77}Ni_6Sn_{10}P_7$ alloy, J. Appl. Phys. 117 (2015) 023109.

[32] W. Zhang, G.H. Cheng, Q. Feng, L.M. Cao, F.P. Wang, R.Q. Hui, Abrupt transition from wavelength structure to subwavelength structure in a single-crystal superalloy induced by femtosecond laser, Appl. Surf. Sci. 257 (2011) 4321–4324.

[33] G.J. Zhang, D.H. Gu, F.X. Gan, X.W. Jiang, Q.X. Chen, Femtosecond laser-induced crystallization in amorphous $Ge_2Sb_2Te_5$ films, Thin Solid Films 474 (2005) 169–172.

[34] B.Q. Chen, Y. Li, Y. Cai, R. Li, S.J. Pang, T. Zhang, Surface vitrification of alloys by laser surface treatment, J. Alloys Compd. 511 (2012) 215–220.

[35] S. Valette, P. Steyer, L. Richard, B. Forest, C. Donnet, E. Audouard, Influence of femtosecond laser marking on the corrosion resistance of stainless steels, Appl. Surf. Sci. 252 (2006) 4696–4701.

[36] A.M. Kietzig, S.G. Hatzikiriakos, P. Englezos, Patterned superhydrophobic metallic surfaces, Langmuir 25 (2009) 4821–4827.

[37] C.C. Yu, J.P. Chu, C.M. Lee, W. Diyatmika, M.H. Chang, J.Y. Jeng, Y. Yokoyama, Bending property enhancements of $Zr_{55}Cu_{30}Al_{10}Ni_5$ bulk metallic glass: effects of various surface modifications, Mater. Sci. Eng. A 633 (2015) 69–75.

[38] J. Bonse, J. Krüger, Pulse number dependence of laser-induced periodic surface structures for femtosecond laser irradiation of silicon, J. Appl. Phys. 108 (2010) 034903.

[39] C. Smith, S. Katakam, S. Nag, X. Chen, R.V. Ramanujan, N.B. Dahotre, et al., Improved soft magnetic properties by laser de-vitrification of Fe-Si-B amorphous magnetic alloys, Mater. Lett. 122 (2014) 155–158.

[40] J.Z.P. Skolski, G.R.B.E. Römer, J.V. Obona, V. Ocelik, A.J. Huis, J.T.M. De Hosson, Inhomogeneous absorption of laser radiation:trigger of LIPSS formation, J. Laser Micro Nanoeng. 8 (2013) 1–5.

[41] S. Vilain, J. Ebothe, M. Troyon, Surface roughness and composition effects on the magnetic properties of electrodeposited Ni-Co alloys, J. Magn. Magn. Mater. 157-158 (1996) 274–275.

[42] G. Palasantzas, J.T.M. De Hosson, Influence of surface roughness on the adhesion of elastic films, Phys. Rev. E: Stat. Nonlinear Soft Matter Phys. 67 (2003) 021604.

[43] Z.P. Lu, C.T. Liu, J.R. Thompson, W.D. Porter, Structural amorphous steels, Phys. Rev. Lett. 92 (2004) 245503.

[44] M.J. Duarte, J. Klemm, S.O. Klemm, K.J.J. Mayrhofer, M. Stratmann, S. Borodin, A.H. Romero, M. Madinehei, D. Crespo, J. Serrano, S.S.A. Gerstl, P.P. Choi, D. Raabe, F.U. Renner, Element-resolved corrosion analysis of stainless-type glass-forming steels, Science 341 (2013) 372–376.

[45] V. Ponnambalam, S.J. Poon, G.J. Shiflet, V.M. Keppens, R. Taylor, G. Petculescu, Synthesis of iron-based bulk metallic glasses as nonferromagnetic amorphous steel alloys, Appl. Phys. Lett. 83 (2003) 1131–1133.

[46] V. Ponnambalam, S.J. Poon, G.J. Shiflet, Fe–Mn–Cr–Mo–(Y,Ln)–C–B (Ln = Lanthanides) bulk metallic glasses as formable amorphous steel alloys, J. Mater. Res. 19 (2004) 3046–3052.

[47] W.C. Oliver, G.M. Pharr, An improved technique for determining hardness and elastic modulus using load and displacement sensing indentation experiments, J. Mater. Res. 7 (1992) 1564–1583.

[48] T. Ahn, S. Oh, X. Hu, J.W. Lee, C.W. Park, H.M. Yang, C. Kim, J.D. Kim, Controlled self-assembly for high-resolution magnetic printing, Small 10 (2014) 1081–1085.

[49] S. He, J.J.J. Nivas, K.K. Anoop, A. Vecchione, M. Hu, R. Bruzzese, S. Amoruso, Surface structures induced by ultrashort laser pulses: formation mechanisms of ripples and grooves, Appl. Surf. Sci. 353 (2015) 1214–1222.

[50] S.M. Eaton, H. Zhang, P.R. Herman, F. Yoshino, L. Shah, J. Bovatsek, A.Y. Arai, Heat accumulation effects in femtosecond laser-written waveguides with variable repetition rate, Opt. Express 13 (2005) 4708–4716.

[51] M. Eisenbach, D.M. Nicholson, A. Rusanu, G. Brown, First principles calculation of finite temperature magnetism in Fe and Fe_3C, J. Appl. Phys. 109 (2011) 07E138.

[52] V.A.M. Brabers, Comment on size-dependent Curie temperature in nanoscale $MnFe_2O_4$ particles, Phys. Rev. Lett. 68 (1992) 3113.

[53] V.I. Maksimochkin, R.R. Gubaidullin, M. Ya, Gareeva Magnetic properties and structure of $Fe_{2-x}Mg_xCrO_4$ chromites, Moscow Univ. Phys. Bull. 68 (2013) 241–248.

[54] J. Adamcik, A. Berquand, R. Mezzenga, Single-step direct measurement of amyloid fibrils stiffness by peak force quantitative nanomechanical atomic force microscopy, Appl. Phys. Lett. 98 (2011) 193701.

[55] C. Walter, C. Mitterer, 3D versus 2D finite element simulation of the effect of surface roughness on nanoindentation of hard coatings, Surf. Coat. Technol. 203 (2009) 3286–3290.

[56] J.Y. Kim, S.K. Kang, J.J. Lee, J.I. Jang, Y.H. Lee, D. Kwon, Influence of surface-roughness on indentation size effect, Acta Mater. 55 (2007) 3555–3562.

4. Further insights into coating formation on iron-based alloys and development of highly porous Fe-Mn-O foams

Chapter 5: General discussion

Chapter 4: Further insights into coating formation on iron-based alloys and development of highly porous Fe-Mn-O foams

In the previous chapter, Fe-based metallic alloys with the conventional fully dense architecture or consisting of a 3D interconnected porous framework are prepared to be used in biomedical and environmental applications. In section 3.1, we showed results on two novel Fe-Mn-Si-Pd biodegradable alloys and on how to adjust their ferromagnetic (including non-ferromagnetic) response by tuning the Mn content. In section 3.2, the Fe-30Mn6Si1Pd alloy was produced by powder metallurgy using a space holder material to obtain an open-cell porous framework with better degradation performance than its bulk counterpart. In section 3.3, porous FeCu alloy prepared by dealloying was found to be an effective Fenton catalyst for water remediation. In Section 3.4, pulsed laser irradiation was used for surface modification of a Fe-based alloy to obtain superhydrophobic surfaces by adjusting both the topological damage as well as the composition of the alloy at surface level.

In this Chapter 4, supplementary works also dealing with Fe-based multifunctional materials and thematically connected with Chapter 3 are presented.

Calcium phosphate (CaP) coatings deposited on Fe-10Mn6Si1Pd alloys by pulsed current electrodeposition are presented in section 4.1. The final goal of this work was to improve the adhesion between the bone and the surrounding tissue, hence enhancing its biocompatibility. Our study reveals that the morphologies of CaP range from needle- to plate-like structures depending on the electrodeposition parameters and the resulting phases. The Young's modulus and hardness values of the electrodeposited coatings are lower than those reported for fully-dense HAp, independently of the deposition conditions, because of the porous morphology of the coatings. However, a good adhesion of the CaP coatings to the substrate is revealed by scratch testing.

Apart from Fe-based 3D interconnected metal porous frameworks (reported in section 3.2 and 3.3), porous inorganic Fe-Mn-O oxide foams are described in section 4.2. Different open cell foams (Fe and Fe-Mn oxides) with low density and homogeneous open-cell structure are prepared from metallic Fe and Mn powder precursors by the replication method using porous polyurethane templates. This study reveals that the magnetic response of the foams, from practically non-magnetic to soft ferrimagnetic, can be tailored by adjusting the Mn content as well as the N_2 flow rate.

For consistency with Chapter 3, sub-chapters 4.1 and 4.2 are structured in the form of articles. The references are thus given at the end of each article.

4.1 Mechanical behaviour of brushite and hydroxyapatite coatings electrodeposited on newly developed FeMnSiPd alloys

Calcium phosphate coatings (CaP) (i.e., brushite and hydroxyapatite) were grown by pulsed current electrodeposition on FeMnSiPd alloys, a newly developed material proposed for biomedical implants. The electrolytic baths contained $Ca(NO_3)_2{\cdot}4H_2O$ and $NH_4H_2PO_4$ as precursors. Bath additives, such as H_2O_2 and NaOH, were used to promote hydroxyapatite (HAp) coating formation directly from the bath. The effect of the electrodeposition parameters on the structure, morphology and mechanical performance of the coatings was investigated. Increasing the electrodeposition time from 900 s to 3600 s resulted in an increase of HAp over the dominant brushite structure. Addition of 0.1 g of NaOH or 3000 ppm of H_2O_2 also promoted an increase of HAp fraction when compared to the coatings obtained from the additive-free bath. Nonetheless, pure HAp was only achieved with the addition of 0.2 g of NaOH to the electrolyte. The morphologies of the CaP particles in the coatings ranged from needle- to plate-like structures depending on the electrodeposition parameters and the resulting phases. The mechanical behaviour of the coatings was studied by scratch testing and nanoindentation. As a general trend, the Young's modulus and hardness values of the electrodeposited coatings were lower than those reported for fully-dense HAp, independently of the deposition conditions, because of the porous morphology of the coatings. No signs of cracking or delamination were observed during nanoindentation or scratch tests except for the coating prepared form the electrolyte containing 3000 ppm of H_2O_2.

4.1.1 Introduction

In recent years, there has been an increasing interest for new biodegradable metallic alloys that fulfil the requirements to be used as temporary medical implants. Within this scenario, Fe-based alloys have gained increasing attention because of the good preliminary results obtained in *in-vitro* and *in-*

vivo experiments [1,2]. For instance, recent studies showed that FeMn [3-9], FeMnPd [3,4], and FeMnSi [7] systems exhibit viable degradation rates and mechanical properties similar to those of 316L stainless steel. In particular, in our previous study on Fe-10Mn-6Si-1Pd alloy, a hardness value around 5.6 GPa and a reduced Young's modulus of 125 GPa were reported [8]. Concerning biocompatibility, the alloy showed good initial cell adhesion. However, the pronounced ion release due to the formation of a cracked, loosely attached superficial oxide layer, hampered the cell proliferation on the surface of this alloy [8].

The development of ceramic coatings such as hydroxyapatite (HAp) or other various forms of calcium phosphates (CaP) on titanium and its alloys [9-12], stainless steel [13,14] and Mg-based alloys [15-17] has been documented to increase their biocompatibiliby [18,19]. This is possible since the bone can form direct chemical bonding to the bioactive CaP, without the occurrence of fibrous interface layers after implantation, which render poor mechanical stability between the implant and the bone. Moreover, in Mg-based alloys, where the main problem for their use as temporary implants are their exceedingly fast degradation rates and the occurrence of high amounts of degradation products (such as Mg^{2+}, H_2 and OH^-), the growth of CaP coatings has proven to be an effective way to increase their corrosion resistance, hence retarding their degradability [15].

The methods used so far to deposit HAp onto metallic alloys include: plasma spraying [20], sputtering [21], pulsed laser-deposition [22], sol-gel [23], and electrochemical deposition [9-14]. Among them, electrodeposition turns out to be a suitable technique to grow uniform coatings with tuneable thickness and chemical composition on complex shaped structures at low temperature and relatively low processing costs. By adjusting the pH, the calcium to phosphorus ratio, the deposition temperature and additives content, the resulting degree of crystallinity, crystalline phases and the preferred orientation (texture), can be tailored. However, it has been reported that direct current electrodeposition usually results in loosely attached deposits to the substrate. To overcome this issue, pulsed electrodeposition has been established as a suitable alternative to grow well-adhered, high-quality HAp coatings [13-15].

While many studies focus on the synthetic strategies to obtain reliable CaP coatings by various methods, fewer efforts have been made to study the mechanical and adhesion properties of these coatings to the substrate. Nanoindentation is the most suitable technique to assess the mechanical properties and the adhesion of thin films. This technique has been recently applied to study the mechanical properties of CaP on stainless steel [24,25], magnesium alloys [26] and titanium [27-29]. However, to the best of our knowledge, there is no data available in the literature on the mechanical properties of CaP coatings grown by electrodeposition onto Fe-based alloys. The substrate type as well as the roughness of the coating may have an influence on the resulting mechanical performance of the studied material. Hence, a detailed mechanical characterization is essential to understand and optimize the properties of Fe-based alloys coated with suitable bioactive materials. The aim of this work is thus to establish an efficient synthetic protocol to produce CaP coatings with good mechanical and adhesion properties on a newly developed Fe-10Mn-6Si-1Pd alloy.

4.1.2 Methods

Cylindrical rods of 3 mm in diameter and 3-4 cm in length with a nominal composition Fe-10Mn-6Si-1Pd (wt.%) were produced following the procedure described elsewhere [8]. Disks of 0.5 mm thickness were cut from the as-cat rod and used as substrates for the CaP deposition. In order to conveniently hold the substrates whilst providing electrical connection, metallic contacts were welded to the backside of the disks, which were subsequently embedded in cold resin. A polishing procedure with abrasive paper up to 4000 grit was then applied until a smooth metallic surface was exposed to view. The surface was ultrasonically cleaned for 5 min in ethanol prior to deposition. The CaP deposition was carried out in a single compartment, double-walled cell with a typical three-electrode configuration (connected to an Autolab 302N potentiostat/ galvanostat). A double junction Ag/AgCl with 3 M KCl inner solution and 1 M NaCl outer solution was used as reference electrode, while a Pt wire was used as counter-electrode. The electrolyte solution was prepared by mixing 0.042 mol/L of $Ca(NO_3)_2 \cdot 4H_2O$ and 0.025 mol/L of $NH_4H_2PO_4$ in Milli-Q water (pH = 4.05). In some cases, 3000 and 4000 ppm of H_2O_2 and 0.1 and 0.2 g of NaOH were added to the electrolyte to favour HAp formation. The deposition was carried out at 65ºC under stirring. Pulsed current electrodeposition with a peak pulse current density of 0.75 mA/cm^2 and t_{ON} = 1s and t_{OFF} = 2s was implemented. The overall deposition time ranged from 900 s to 3600s. For comparison purposes, direct current (DC) electrodeposition was carried out at 0.75 mA/cm^2 for 1200s. To promote the brushite to HAp transformation, some specimens were rinsed in 0.1M NaOH solution for 72 h at room temperature.

Scanning electron microscopy (SEM) using a Zeiss Merlin microscope equipped with an energy dispersive X-ray (EDX) detector was used for morphological and compositional analyses. X-ray diffraction (XRD) was carried out using a Philips X'Pert diffractometer with Cu Kα radiation. The measurements were performed in the angular range 2□ = 10–60º with a step size of 0.026º.

The thickness of the coatings deposited on the Fe-10Mn-6Si-1Pd substrates was evaluated with a 3D Optical Surface Metrology System (DCM 3D) from Leica which combines confocal and interferometry technology.

Nanoindentation and scratch experiments were performed using a Nanoindenter XP from MTS equipped with a Berkovich tip. The nanoindentation function consisted of a loading segment of 30 s, followed by a load holding segment of 10 s and an unloading segment of 30 s. The maximum applied load was set to 5 mN and 100 mN (two sets of experiments). The thermal drift was kept below ± 0.1 nm/s. From the load-displacement curves, the hardness and reduced Young's modulus values were derived using the method of Oliver and Pharr [30]. Scratch tests were carried out applying an increasing normal load with the option for lateral force measurements. The normal load was linearly swept from 0 to 100 mN along the length of the scratch (500 µm) at a scratch velocity of 10 µm/s. The tests were repeated three times for each electrodeposition condition. Prior to scratch, an initial profile at 10 µN at the location where the scratch will be performed was carried out to assess the surface morphology. The actual penetration depth of the indenter under the sample surface was estimated by comparing the indenter displacement normal to the surface during scratching with the topography of the original surface at each position along the scratch length. For the scratch segment, the roughness and the slope of the surface were considered in the calculation of the indenter penetration. After the scratch, in a similar manner, a final profile was recorded to establish the residual scratch depth.

4.1.3 Results and Discussion

4.1.3.1 Morphological and Structural characterization

Figure 4.1.1a shows the XRD patterns of the as-deposited coatings on Fe-10Mn-6Si-1Pd alloy at a pulsed current density of 0.75 mA/cm^2 for 900, 1800 and 3600 s from the electrolytic bath without additives. The XRD patterns reveal that the main phase of the as-deposited coatings, independently of the deposition time, is the dicalcium phosphate dihydratate (Brushite, $CaHPO_4{\cdot}2H_2O$) with minor content of hydroxyapatite (HAp, $Ca_{10}(PO_4)_6(OH)_2$). However, the peaks belonging to HAp gain intensity as the deposition time increases. The intensity ratio between the (020) peak belonging to brushite (at 2θ = 11.70º) and the (002) peak belonging to HAp (at 2θ = 25.9º) is listed in Table 4.1.1, as an indicative parameter for the predominant phase formation. The growth of HAp (and its predominance over brushite) can be explained by the chemical and electrochemical reactions that occur during the deposition process. The main reactions are listed below:

$$2H_2O + 2e^- = H_2 + 2OH^- \quad (1)$$

$$O_2 + 2H_2O + 4e^- = 4OH^- \quad (2)$$

$$2H_2PO_4^- + 2e^- = HPO_4^{2-} + H_2 \quad (3)$$

$$Ca^{2+} + HPO_4^{2-} + 2H_2O \rightarrow CaHPO_4 \cdot 2H_2O \quad (4)$$

It has been widely accepted that OH^-anions and H_2 gas bubbles are produced around the working electrode as a result of the reduction of oxygen and/or water (Eqs. 1 and 2), hence causing an increase of pH around the metal/solution interface [13]. However, at the beginning of the deposition process, the increase of pH is not enough to facilitate the formation of HAp, which is stable in the 9.5 to 12 pH range. On the contrary, brushite deposition is favored over HAp as $\mathrm{HPO_4^{2-}}$, which is reduced from $\mathrm{H_2PO_4^-}$ (Eq. 3), combines with $\mathrm{Ca^{2+}}$and $\mathrm{H_2O}$ to form $\mathrm{CaHPO_4 \cdot 2H_2O}$ (Eq. 4), the kinetically stable CaP in acidic conditions. $\mathrm{HPO_4^{2-}}$ also reduces to yield $\mathrm{PO_4^{3-}}$ (Eq. 5); however, at the beginning of the electrodeposition process, the concentration of $\mathrm{OH^-}$ is not large enough to enable the formation of HAp [13].

$$\mathrm{2HPO_4^{2-} + 2e^- = 2PO_4^{3-} + H_2} \qquad (5)$$

$$\mathrm{10Ca^{2+} + 6PO_4^{3-} + 2OH^- \rightarrow Ca_{10}(PO_4)_6(OH)_2} \qquad (6)$$

Nonetheless, as deposition time increases, a decrease in the deposition potential is experimentally observed (from -0.68 V to -1.1 V) because of the formation and growth of the insulating CaP layer. This lower potential will result in the electrogeneration of a larger amount of $\mathrm{OH^-}$ ions, which will induce a local increase of the pH at the electrode interface, hence, favouring the growth of HAp (eq. 6). In fact, the increase of pH due to the formation of OH^- ions in the vicinity of the cathode induced by high cathode current densities (i.e. 2, 3, 10 mA/cm^2) has been extensively reported [13,15].

Additives	time	$I_{\text{Brushite (020) peak}}/I_{\text{HAp (002) peak}}$
-	900	141
-	1800	36.6
-	3600	23
3000 ppm H_2O_2	3600	1.11
4000 ppm H_2O_2	3600	3.86
0.1 g NaOH	3600	15

Table 4.1.1: Ratio between the experimental intensities of the (020) peak from brushite and the (002) peak from HAp.

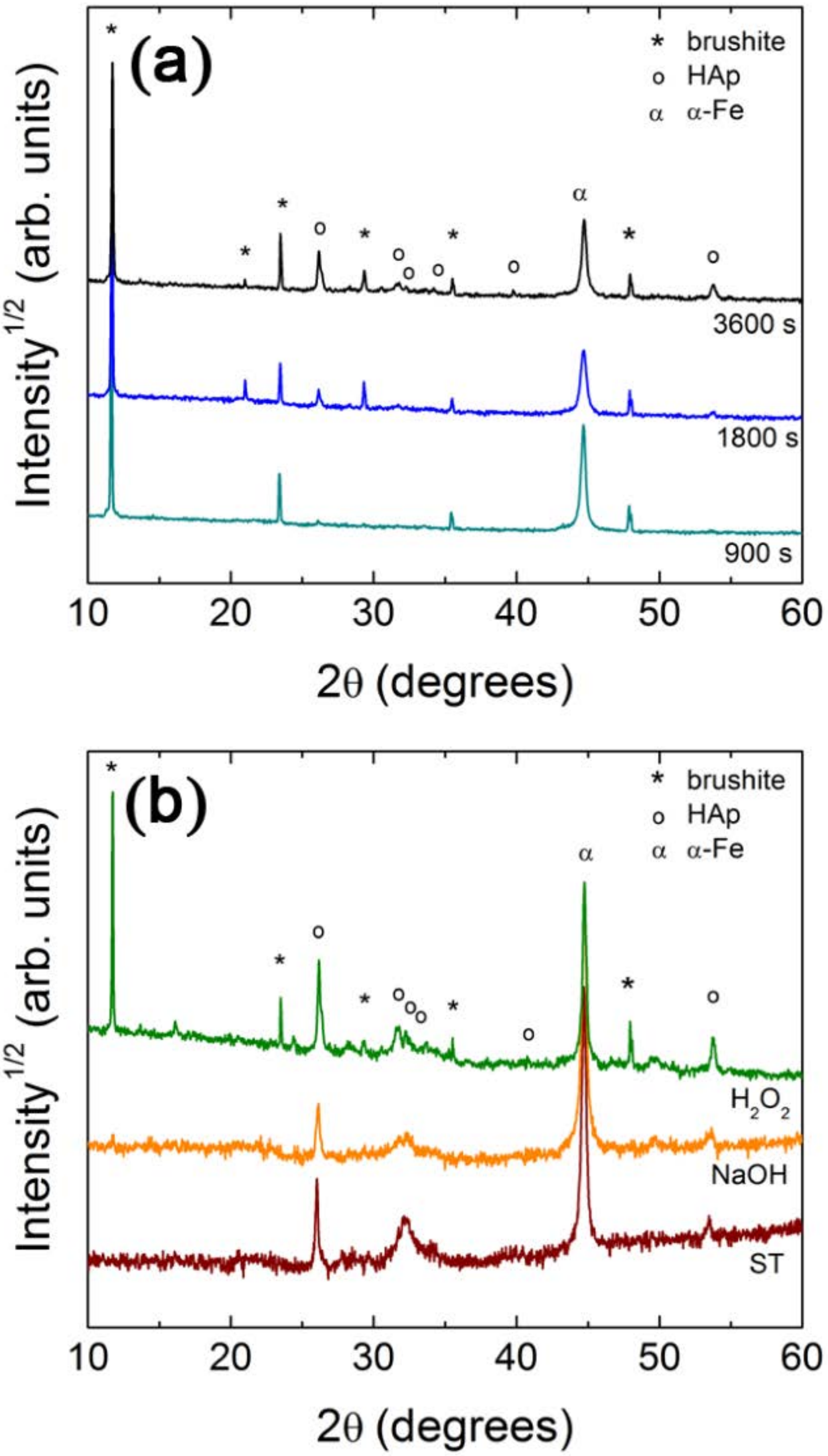

Figure 4.1.1: X-ray diffraction patterns of pulse-plated coatings on Fe-10Mn-6Si-1Pd alloys produced from: (a) the additive-free bath (no additives, NA curve) for 900 s, 1800 s and 3600 s, (b) the bath containing 3000 ppm of H_2O_2 (H_2O_2 curve) for 3600 s, the bath containing 0.2 g of NaOH (NaOH curve) for 3600 s, and the additive-free bath for 3600 s followed by solution treatment (ST curve) with 0.1 M NaOH for 72 h.

In order to accelerate the direct formation of HAp on Ti-, Mg-, and Fe-based alloys (i.e., with no need of additional thermal treatments) various approaches have been followed. For instance, some works reported that the addition of H_2O_2 into the electrolyte acts as an alternative electrochemical source of OH^- ions which can then promote the formation of HAp over other CaP species [13,31,32]. With this purpose, 3000 and 4000 ppm of H_2O_2 were added to the electrolyte. The addition of 3000 ppm of H_2O_2 results in an increase of the XRD peaks belonging to HAp although brushite is still present in the coating (Figure 4.1.1b). Increasing the amount of H_2O_2 to 4000 ppm does not further rise the HAp content (Table 4.1.1); furthermore, the surface of the alloy becomes partially covered by an orange layer attributed to oxides. The second approach to obtain pure HAp was to increase the pH of the electrolyte by the addition of NaOH. The addition of 0.1 g of NaOH (pH = 5.05) results in a mixture of brushite and HAp phases, similar to the results obtained with 3000 ppm or 4000 ppm of H_2O_2 (Table 4.1.1). The addition of 0.2 g of NaOH increases the pH of the electrolyte to 8.5. In this case, as it can be observed in the XRD pattern (Figure 4.1.1b), the coating only consists of HAp. Pure HAp is also obtained from an as-deposited mixture of brushite and HAp by solution treatment in 0.1 M NaOH for 72 h at room temperature (Figure 4.1.1b).

At first glance, the coatings produced by pulsed-current deposition are well adhered to the Fe-10Mn-6Si-1Pd substrate and the whole surface is homogeneously covered by HAp and/or brushite. However, the adhesion of the coatings grown by direct current deposition for 1200 s was not satisfactory and some parts peeled-off during handling, so no further characterization was carried out in this case.

It is worth noticing that different morphologies can be observed depending on the resulting phases and deposition conditions. When the coating is formed by a mixture of brushite and HAp (i.e., the coatings produced without additives, with 3000 ppm of H_2O_2 or with 0.1 g of NaOH), a morphology mainly consisting of thin rods or needles oriented perpendicular or tilted with respect to the sample's surface can be observed (Figures 4.1.2a and 4.1.2b). Some zones are covered with thicker disordered rods, particularly for shorter deposition times (i.e. 900 and 1800 s) (Figure 4.1.2a). The EDX analysis corresponding to short deposition times (Figure 4.1.2e), reveals that the ratio between Ca and P is approximately 1.05. This ratio is very close to the 1.0 ratio typically observed for stoichiometric brushite, thus indicating that the zones covered with thicker disordered threads mainly consist of brushite. Conversely, a larger Ca/P ratio of 1.25 (Figure 4.1.2f) is detected in the zones consisting of thin threads (i.e., longer electrodeposition times). The increase of the Ca/P ratio can be indicative of HAp formation, probably on top of brushite. These observations are thus in agreement with the XRD results (Figure 4.1.1a).

In turn, SEM imaging reveals that the coating produced from the electrolyte containing 0.2 g of NaOH exhibits a plate-shaped morphology (Figure 4.1.2c) characteristic of HAp formation. The plates are hexagonal-shaped with preferred a (b)-axis orientation with an average size of ~2 μm. The Ca/P ratio, equal to 1.31 (Figure 4.1.2g), is lower than the 1.67 value characteristic for the stoichiometric HAp, thus suggesting the formation of calcium-deficient HAp (CDHAp). Ca/P ratios between 1.31 and 1.67 were also observed by other authors and related these values to the chemical reactions occurring during the growth of the coatings [33,34]. The TEM image of this coating, shown in Figure 4.1.3a, confirms the plate-like morphology typical of HAp. In agreement with the theoretical diffraction pattern of HAp (Ref. Code 00-011-0293), several interplanar distances can be calculated from the SAED pattern of Figure 4.1.3b. For the sake of clarity, only the most intense diffraction spots/rings have been indexed in the figure.

Finally, the morphology observed in the coating after being immersed in 0.1M NaOH solution for 72 h (Figure 4.1.2d) is similar to the morphology observed for as-deposited coatings for 900 and 1800 s. However, in this case the Ca/P ratio is closer to the theoretical value of 1.67, typical of stoichiometric HAp.

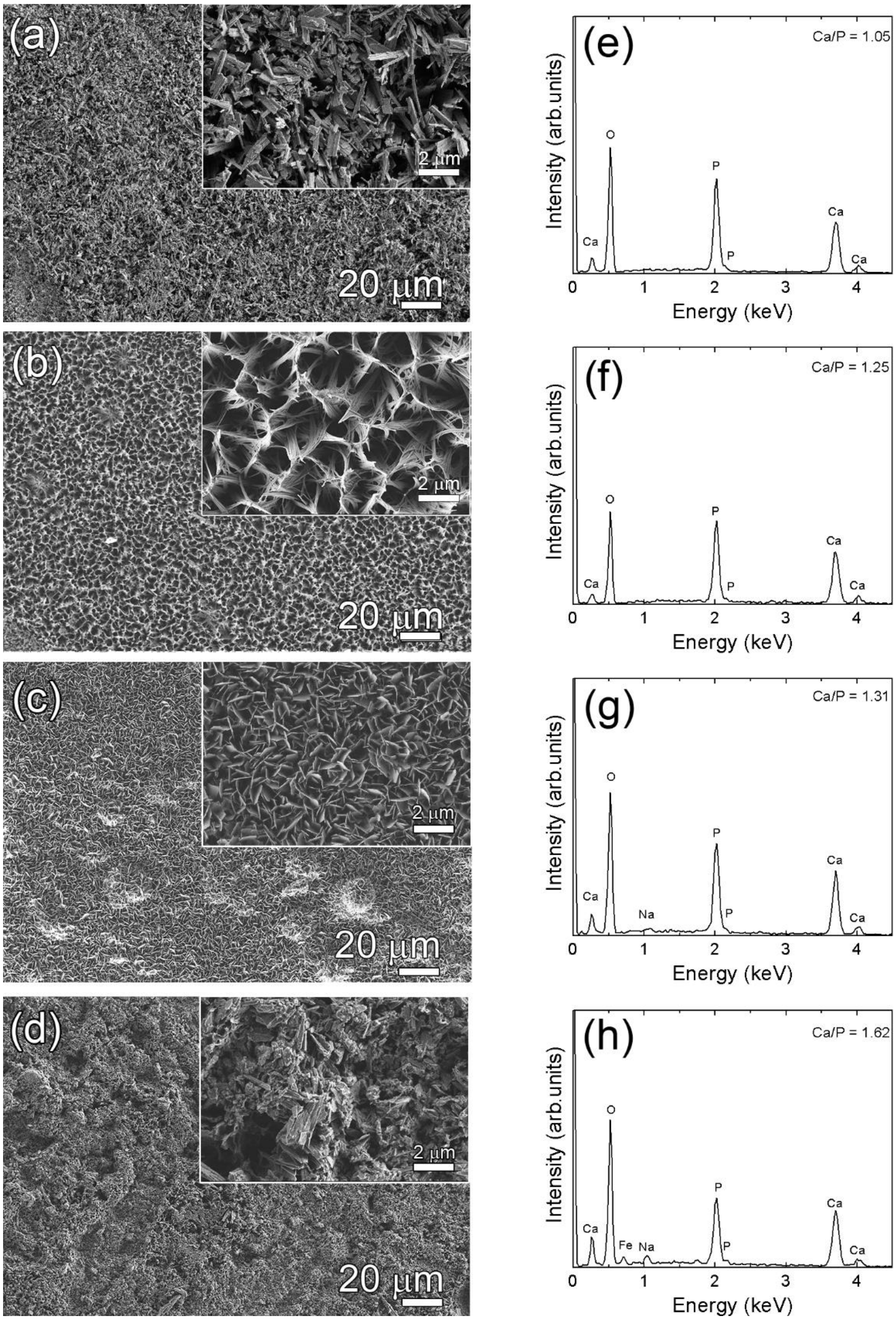

Figure 4.1.2: SEM images of coatings produced from: (a) the additive-free bath for 1800 s, (b) the additive-free bath for 3600 s, (c) the bath containing 0.2 g of NaOH for 3600 s and (d) the additive-free bath for 3600 s and solution treated with 0.1 M NaOH for 72 h. The insets are higher magnifications SEM images. (e), (f), (g) and (h) are the EDX spectra corresponding to the areas depicted in (a), (b), (c) and (d), respectively.

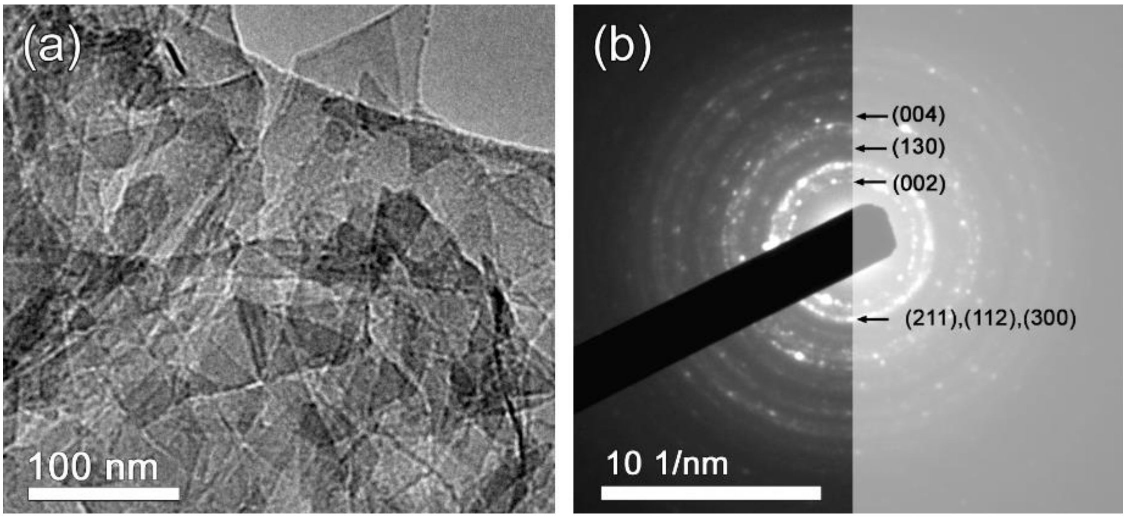

Figure 4.1.3: (a) TEM image of the coating produced from the bath containing 0.2 g of NaOH for 3600 s, (b) corresponding SAED pattern.

4.1.3.2 Mechanical Characterization

It is well-known that one of the drawbacks of CaP coatings prepared by DCelectrodeposition is that their adherence to the underlying substrate is not sufficiently strong [13,15,35]. As a result, pulsed current electrodeposition has emerged as a more suitable technique to obtain well-adhered coatings. So far, the mechanical properties of CaP coatings (including HAp) produced by electrodeposition have not been studied in detail. Nanoindentation is a versatile technique that can be used to measure film adhesion; either from transverse scratching or by direct indentation [36]. Both approaches are used in this work to assess the mechanical properties of the coatings. Direct indentation is employed to evaluate the hardness, Young's modulus and plastic energy values of the CaP coatings and Fe-10Mn-6Si-1Pd substrate, while scratch tests are utilized to assess the adhesion of the layers to the substrate. Note that in this work a few CaP coatings were prepared by DC electrodeposition but their poor adhesion to the substrates resulted in peeling-off of some parts of the films during handling; henceforth, no further characterization was carried out. Only the coatings prepared by pulsed electrodeposition were investigated in detail by mechanical means.

4.1.3.2.1 Indentation tests

Indentation measurements (Figure 4.1.4) were carried out for the coatings deposited for 3600 s from the additive-free bath (NA), from the bath containing 3000 ppm of H_2O_2 (curve denoted as H_2O_2), from the bath containing 0.2 g of NaOH (curve labelled as NaOH) and from the as-deposited coating produced from the additive-free electrolyte but subsequently solution treated with 0.1 M NaOH for 72 h (curve labelled as ST) to study the influence of the different phases and the synthetic parameters on the resulting mechanical properties. A summary of the mechanical properties is presented in Table 4.1.2. Nanoindentation is a suitable technique to measure the mechanical properties of thin films; however, to avoid unintentional influence from the properties of the substrate, it is commonly accepted that the maximum penetration depth should be lower than 1/10th of the overall film thickness [36]. The indentation curves presented in Figures 4.1.4a and 4.1.4b were carried out using a maximum applied load of 5 mN and 100 mN, respectively. Notice that the maximum penetration depth exceeds the 10 % of the film thickness, even for P_{Max} = 5 mN (see Table 4.1.2). Thus, the Young's modulus and hardness values are influenced to some extent by the mechanical response of the substrate. Nonetheless, as can be observed in Table 4.1.2, the Young's modulus and hardness values of the substrate are much larger than those of the coatings, suggesting a limited contribution from the substrate. Therefore, the obtained values are still a good indicator of the dissimilar mechanical behaviour of the various coatings. Among the four different coatings tested in this work, the H_2O_2 one, which mainly consists of brushite and HAp, is the softest one, followed by the NA coating, which has a similar microstructure than the H_2O_2 one but has a lower HAp content. Several discontinuities can be observed from the load-displacement curve of the NaOH coating recorded up to a maximum applied load of 5 mN. These discontinuities are typically attributed to dislocation activity but, in this particular situation, they are likely due to cracking or bending of the HAp plates, as can be verified by imaging the nanoindentation imprint by SEM (Figure 4.1.5a). The NaOH sample exhibits the largest hardness and Young's modulus values, which can be ascribed to the less porous nature of the coating as a result of the plated-shape morphology. In fact, the low Young's modulus and hardness values reported in this work (compared to the bulk values, i.e., H = 8.5 GPa and E_r = 130 GPa for bulk fully-dense HAp) [37] are mainly attributed to the particular morphology (i.e. plate-/needle-like) of the samples, which can be regarded as surface roughness or porosity [38].

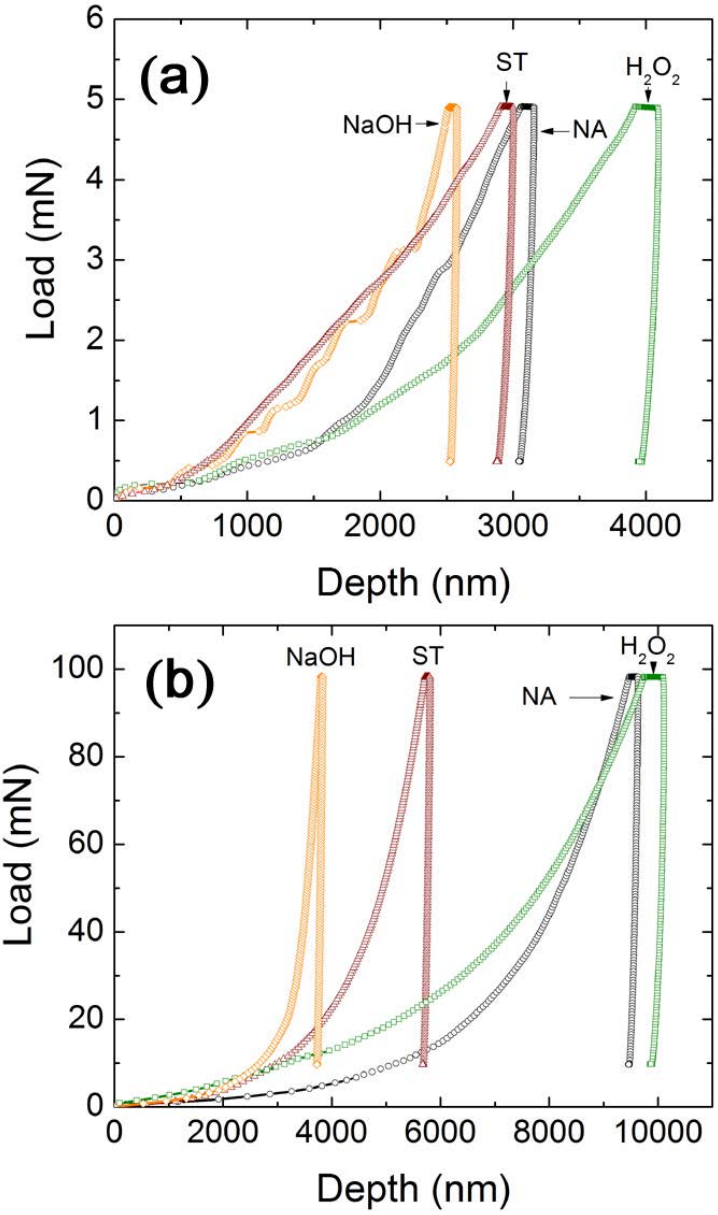

Figure 4.1.4: Load-displacement curves of the coated-Fe-10Mn-6Si-1Pd alloys applying a maximum load of (a) 5 mN and (b) 100 mN. NA stands for the coating obtained from the additive-free bath, H_2O_2 stands for the coating obtained from H_2O_2 containing electrolyte, NaOH applies to the coating produced from NaOH containing electrolyte and ST refers to the coating obtained from the additive-free bath further treated with NaOH at RT for 72 h.

Sample	**Thickness (μm)**	**P_{max} (mN)**	**H (GPa)**	**E_r (GPa)**	**U_{pl}/U_t*100**
Fe-30Mn-6Si-1Pd substrate	2000-3000	5	8.6 ± 0.6	226 ± 15.0	76.0 ± 2.5
		100	5.6 ± 0.4	193 ± 5	82 ± 4
NA	13.4 ± 0.9	5	0.021 ± 0.015	4.5 ± 1.4	95 ± 3
		100	0.050 ± 0.011	21 ± 5	96.5 ± 0.5
H_2O_2	14.4 ± 1.4	5	0.014 ± 0.004	3.1 ± 1.0	97.1 ± 0.9
		100	0.047 ± 0.016	20 ± 6	97.9 ± 0.4
0.2 g NaOH	12.8 ± 0.5	5	0.031 ± 0.009	15 ± 4	97.3 ± 0.3
		100	0.31 ± 0.12	67 ± 9	89.2 ± 1.9
ST	3.3 ± 0.8	5	0.024 ± 0.009	4.7 ± 1.2	95.8 ± 0.7
		100	0.15 ± 0.04	45 ± 7	96.1 ± 1.8

Table 4.1.2: Thickness and mechanical properties of the coatings and the Fe-10Mn-6Si-1Pd substrate measured by nanoindentation applying maximum forces (P_{Max}) of 5mN and 100 mN. H, E_r, U_{pl} and U_t denote the hardness, reduced Young's modulus, plastic indentation energy and total indentation energy, respectively.

In general, the mechanical properties of HAp coatings largely depend on the production technique. For instance, HAp films fabricated by plasma spraying using coarse powders exhibit a Young's modulus of 53-58 GPa [39], while those produced from a solution precursor exhibit a Young's modulus of 5-22 GPa [40]. In addition, He et al. [37] reported that the elastic modulus of fully-dense HAp produced by powder compaction and sintering process is ~130 GPa but it decreases to 20 GPa for a porosity level of 54%. Hence, differences in the elasticity of HAp coatings depend on the dissimilar microstructures that can be obtained using different synthetic pathways. In this work, when the applied load is 5 mN, the Young's modulus ranges from 4.5 to 15 GPa (depending on the microstructure and thickness of the coating). Larger Young's modulus values, from 19.5 to 67 GPa, are observed when the applied load is 100 mN. The same trend is observed for hardness; it increases with the maximum applied load. These trends can be attributed to a larger contribution from the substrate at larger applied loads but also to the densification of the coatings as the indenter penetrates into the material. SEM images of the imprints left behind on the NaOH coating after applying a maximum load of 5 mN and 100 mN are presented in Figure 4.1.5. No cracks or delamination can be observed at any condition, but a much higher compaction is evident when the applied maximum load is 100 mN.

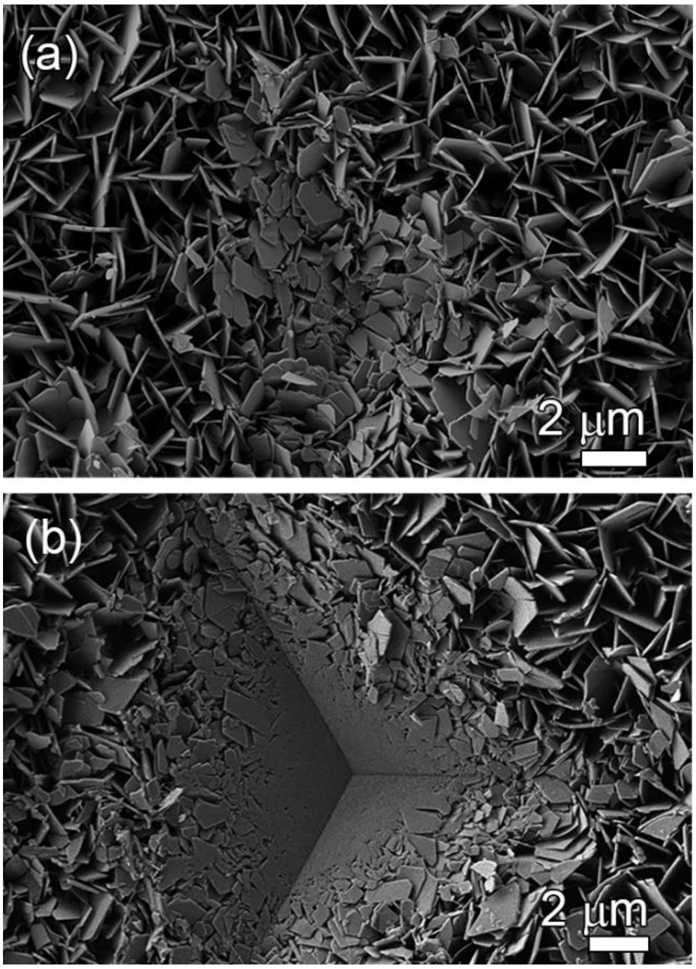

Figure 4.1.5: SEM images of the indentation imprints left on the coating produced from the bath containing 0.2 g of NaOH at a maximum applied load of (a) 5 mN (b) 100 mN.

Nanoindentation can also be used to assess the absorbed/dissipated energy by the specimens during the compressive tests, by comparing the values of the elastic and plastic indentation energies and their ratio. The area enclosed by the loading curve and the displacement axis corresponds to the total indentation energy (U_t). The area below the unloading part of the load-displacement curve and the displacement axis provides the elastic energy (U_e) recovered from the system during unloading. The area enclosed by the loading and unloading curves represents the unrecoverable inelastic or plastic energy ($U_{pl} = U_t - U_e$), related to the work spent during plastic deformation or other irreversible processes (e.g. cracking, crushing or compaction) and the energy stored in the form of residual stresses caused by the resultant impression [37]. The normalized inelastic energy $(U_{pl}/U_t)*100$ is commonly used as an indirect estimation of the energy absorbed by the material. From the nanoindentation curves presented in Figure 4.1.4 and from the $(U_{pl}/U_t)*100$ ratio in Table 4.1.2, it can be seen that the plastic energy is much higher than the elastic energy in all cases, which indicates the essentially plastic behaviour of the coatings. Namely, almost all the deformation caused by the applied load in the coatings is irreversible. This is obviously related to the compaction process that takes places in these materials, as can be observed in Figure 4.1.5.

4.1.3.2.2 Scratch tests

Figure 4.1.6a shows the dependence of the penetration depth as a function of the scratch distance for the different investigated samples. A pronounced decrease of the penetration depth at the beginning of the scratch test is observed in all cases, followed by a less abrupt decrease at higher loads; this exponential decay can be attributed to the soft mechanical behaviour associated with the highly porous morphology and material densification at larger loads. However, some differences can be pointed out among the four samples. The H_2O_2 coating exhibits a larger penetration depth along the entire path. This is due to the larger porosity level associated with the needle-like morphology of this alloy and its consequently lower hardness (Table 4.1.2). In addition, the more abrupt penetration depth drops observed in this sample are also probably associated to the larger number of cracks stemming from the brittle morphology of the coating. Delamination or failure of the coating was not detected by post-scratch SEM imaging; however, a penetration of 15 μm and the sudden drops identified at 300 and 500 μm suggest a possible local failure. The SEM images of the last few microns of the scratches carried out in the H_2O_2 and NaOH coatings (see Figure 4.1.7) reveal the local failure of the H_2O_2 coating. Conversely, only a densification phenomenon can be observed in the SEM image of the scratch performed in the NaOH coating. A maximum depth of ~9 μm is achieved in the NA coating, which is slightly larger than the ~5.5 μm maximum penetration depth for the ST and NaOH samples. At a scratch distance of ~150 μm the penetration does not further increase with the normal force as the densification process has finished and the penetration of the tip is much lower in the fully dense state. The dependence of friction force on the scratch distance is shown in Figure 4.1.6b. The friction force increases linearly with the scratch distance. Larger frictional forces are observed for the NA, ST and H_2O_2 samples but much lower frictional forces, which will result in a lower friction coefficient, are detected for the NaOH coating.

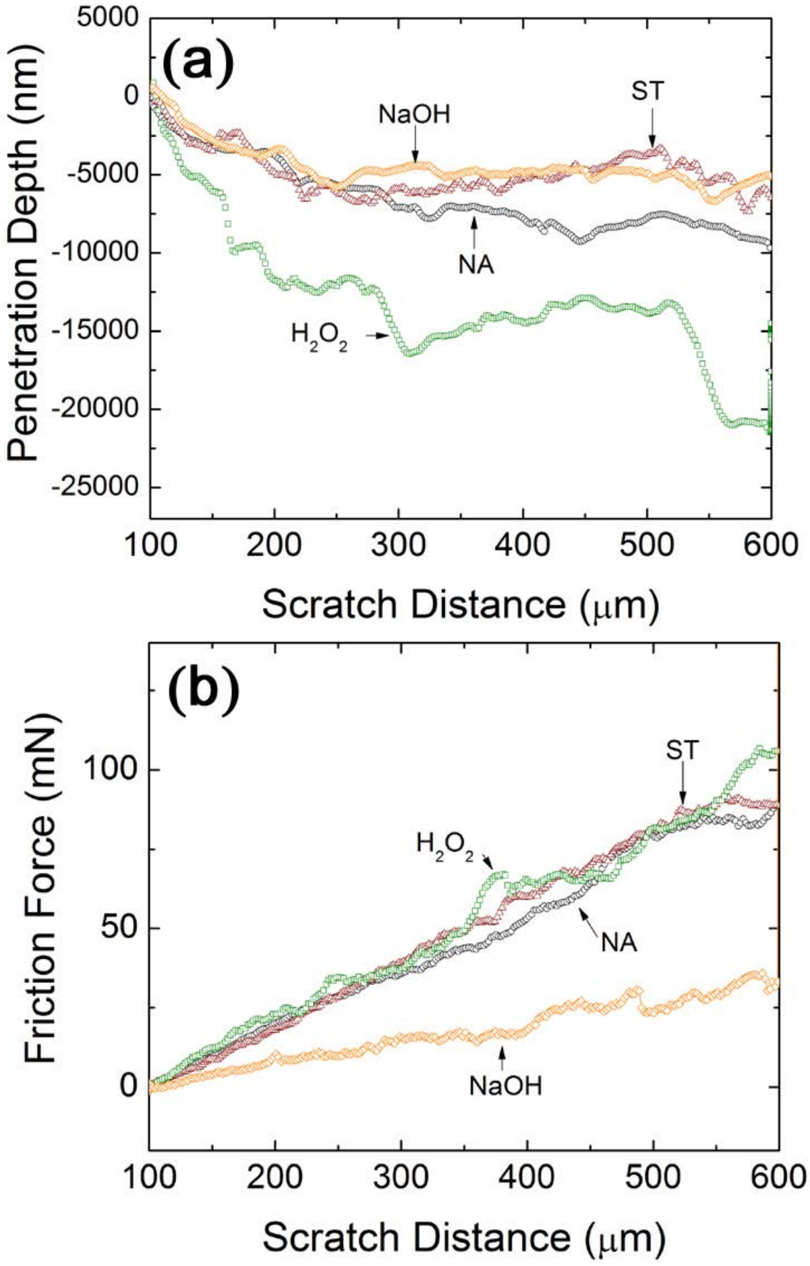

Figure 4.1.6: Scratch tests carried out on the coated-Fe-10Mn-6Si-1Pd alloys showing (a) penetration depth *versus* scratch distance, (b) friction force *versus* scratch distance. The same nomenclature as in Figure 4.1.4 is used.

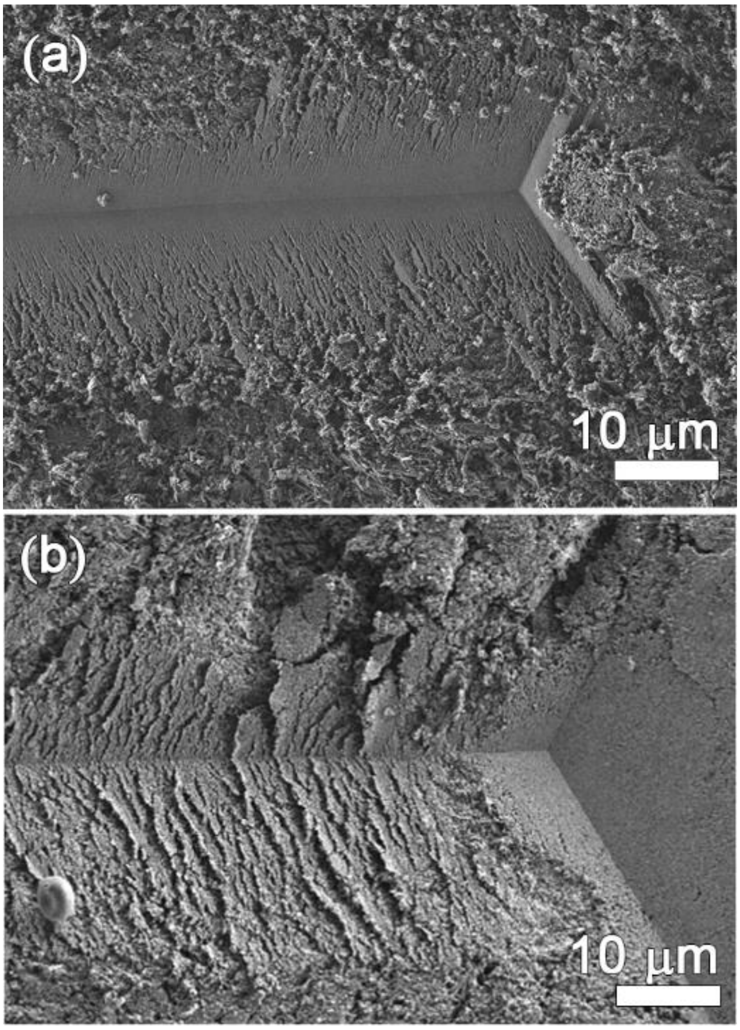

Figure 4.1.7: SEM images of the last few microns of the scratch tests performed on the coatings produced from (a) NaOH containing electrolyte and (b) H_2O_2 containing electrolyte coating.

4.1.4 Conclusions

Well-adhered CaP coatings on FeMnSiPd substrates have been successfully prepared by pulsed current electrodeposition. By tuning the deposition time and the composition of the bath, coatings with different amounts of brushite and HAp phases can be obtained. Electrodeposition of CaP results in needle-, rod- or plate-like morphologies leading to porous coatings. As a result, the measured Young’s modulus and hardness are lower than those of fully-dense coatings with analogous compositions, hence approaching the values of both parameters in cortical bone. If the applied loads are high enough, the porous layers tend to be compacted, leading to an increase in both hardness and Young's modulus. Finally, delamination or failure of the coatings were not detected during scratch tests, thus corroborating the good adherence of the coatings to the Fe-based alloy.

References

[1] R. Waksman, R. Pakala, R. Baffour, R. Seabron, D. Hellinga, F. O. Tio, Short-term effects of biocorrodible iron stents in porcine coronary arteries, Journal of Interventional Cardiology 21 (2008) 15-20.

[2] M. Peuster, C. Hesse, T. Schloo, C. Fink, P. Beerbaum, C. von Schnakenburg, Long-term biocompatibility of a corrodible peripheral iron stent in the porcine descending aorta, Biomaterials 27 (2006) 4955-4962.

[3] M. Schinhammer, A. C. Hanzi, J. F. Loffler, P. J. Uggowitzer, Design strategy for biodegradable Fe-based alloys for medical applications, Acta Biomaterialia 6 (2010) 1705-1713.

[4] F. Moszner, A. S. Sologubenko, M. Schinhammer, C. Lerchbacher, A. C. Hanzi, H. Leitner, P. J. Uggowitzer, J. F. Loffler, Precipitation hardening of biodegradable Fe–Mn–Pd alloys, Acta Materialia 59 (2011) 981-991.

[5] M. Schinhammer, C. M. Pecnik, F. Rechberger, A. C. Hanzi, J. F. Loffler, P. J. Uggowitzer, Recrystallization behavior, microstructure evolution and mechanical properties of biodegradable Fe–Mn–C(–Pd) TWIP alloys, Acta Materialia 60 (2012) 2746-2756.

[6] H. Hermawan, D. Dube, D. Mantovani, Degradable metallic biomaterials: design and development of Fe-Mn alloys for stents, Journal of Biomedical Materials Research Part A 93 (2010) 1-11.

[7] B. Liu, Y. F. Zheng, L. Q. Ruan, In vitro investigation of Fe30Mn6Si shape memory alloy as potential biodegradable metallic material, Materials Letters 65 (2011) 540-543.

[8] Y.P. Feng, A. Blanquer, J. Fornell, H. Zhang, P. Solsona, M.D. Baró, S. Suriñach, E. Ibáñez, E. García-Lecina, X. Wei, R. Li, Ll. Barrios, E. Pellicer, C. Nogués, J. Sort, Novel Fe–Mn–Si–Pd alloys: insights into mechanical, magnetic, corrosion resistance and biocompatibility performances, Journal of Materials Chemistry B 4 (2016) 6402-6412.

[9] K.A. Khor, C.S. Yip, P. Cheang, Ti-6Al-4V/hydroxyapatite composite coatings prepared by thermal spray techniques, Journal of Thermal Spray Technology 6 (1997) 109-115.

[10] A.K. Lynn, D.L. DuQuesnay, Hydroxyapatite-coated Ti–6Al–4V: Part 2: the effects of post-deposition heat treatment at low temperatures, Biomaterials 23 (2002) 1947-1953.

[11] E.A. dos Santos, M.S. Moldovan, L. Jacomine, M. Mateescu, J. Werckmann, K. Anselme, P. Mille, H. Pelletier, Oriented hydroxyapatite single crystals produced by the electrodeposition method, Materials Science and Engineering: B 169 (2010) 138-144.

[12] M.H.P Da Silva, J.H.C. Lima, G.A. Soares, C.N. Elias, M.C. de Andrade, S.M. Best, I.R. Gibson, Bioactivity assessment of hydroxyapatite coatings produced by alkali conversion of monetite, Surface and Coatings Technology 137 (2001) 270-276.

[13] D. Gopi, J. Indira, L. Kavitha, A comparative study on the direct and pulsed current electrodeposition of hydroxyapatite coatings on surgical grade stainless steel, Surface and Coatings Technology 206, (2012) 2859-2869.

[14] G. Blanda, V. Brucato, F.C. Pavia, S. Greco, S. Piazza, C. Sunseri, R. Inguanta, Galvanic deposition and characterization of brushite/hydroxyapatite coatings on 316L stainless steel, Materials Science and Engineering: C 64 (2016) 93-101.

[15] H.X. Wang, S.K. Guan, X. Wang, C.X. Ren, L.G. Wang, In vitro degradation and mechanical integrity of Mg–Zn–Ca alloy coated with Ca-deficient hydroxyapatite by the pulse electrodeposition process, Acta Biomaterialia 6 (2010) 1743-1748.

[16] Y.W. Song, D.Y. Shan, E.H. Han, Electrodeposition of hydroxyapatite coating on AZ91D magnesium alloy for biomaterial application, Materials Letters 62 (2008) 3276.

[17] H.M. Mousa, A.P. Tiwari, J. Kim, S.P. Adhikari, C.H. Park, C.S. Kim, A novel in situ deposition of hydroxyapatite nanoplates using anodization/hydrothermal

process onto magnesium alloy surface towards third generation biomaterials, Materials Letters 164 (2016) 144-147.

[18] M.H.P. Da Silva, G.A. Soares, C.N. Elias, I.R. Gibson, S.M. Best, Transformation of monetite to hydroxyapatite in bioactive coatings on titanium, Key Engineering Materials 192 (2000) 159-162.

[19] R. Rohanizadeh, R.Z. LeGeros, M. Harsono, A. Bendavid, Adherent apatite coating on titanium substrate using chemical deposition, Journal of Biomedical Materials Research Part A 72 (2005) 428-438.

[20] H. Wang, N. Eliaz, Z. Xiang, H.P. Hsu, M. Spector, L.W. Hobbs, Early bone apposition in vivo on plasma-sprayed and electrochemically deposited hydroxyapatite coatings on titanium alloy, Biomaterials 27 (2006) 4192-4203.

[21] Y. Yang, K.H. Kim, J.L Ong, A review on calcium phosphate coatings produced using a sputtering process—an alternative to plasma spraying, Biomaterials 26 (2005) 327-337.

[22] Y. Suda, H. Kawasaki, T. Ohshima, S. Nakashima, S. Kawazoe, T. Toma, Hydroxyapatite coatings on titanium dioxide thin films prepared by pulsed laser deposition method, Thin Solid Films 506 (2006) 115-119.

[23] Y.L. Jeyachandran, S. Venkatachalam, B. Karunagaran, Sa.K. Narayandass, D. Mangalaraj, C.Y. Bao, C.L. Zhang, Bacterial adhesion studies on titanium, titanium nitride and modified hydroxyapatite thin films, Materials Science and Engineering: C 27 (2007) 35-41.

[24] D. Sidane, D. Chicot, S. Yala, S. Ziani, H. Khireddine, A. Iost, X. Decoopman, Study of the mechanical behavior and corrosion resistance of hydroxyapatite sol-gel thin coatings on 316L stainless steel pre-coated with titania film, Thin Solid Films 593 (2015) 71-80.

[25] Mina, A. Castaño, J.C. Caicedo, H.H. Caicedo, Y. Aguilar, Determination of physical properties for β-TCP + chitosan biomaterial obtained on metallic 316L substrates, Materials Chemistry and Physics 160 (2015) 296-307.

[26] M.A. Surmeneva, A.I. Tyurin, T.M. Mukhametkaliyev, T.S. Pirozhkova, I.A. Shuvarin, M.S. Syrtanov, R.A. Surmenev, Enhancement of the mechanical properties of AZ31 magnesium alloy via nanostructured hydroxyapatite thin films fabricated via radio-frequency magnetron sputtering, Journal of the Mechanical Behavior of Biomedical Materials 46 (2015) 127-136.

[27] H.Wang, C.J. Lin, R. Hu, F. Zhang, L.W. Lin, A novel nano-micro structured octacalcium phosphate/ protein composite coating on titanium by using an electrochemically induced deposition, Journal of Biomedical Materials Research Part A 87 (2008) 698-705.

[28] X. Bai, S. Sandukas, M. R. Appleford, J.L. Ong, A. Rabiei, Deposition and investigation of functionally graded calcium phosphate coatings on titanium, Acta Biomaterialia 5 (2009) 3563-3572.

[29] R. Drevet, N. Ben Jaber, J. Fauré, A. Tara, A. Ben Cheikh Larbi, H. Benhayoune, Electrophoretic deposition (EPD) of nano-hydroxyapatite coatings with improved mechanical properties on prosthetic Ti6Al4V substrates, Surface and Coatings Technology 301, (2016) 94-99.

[30] W.C. Oliver, G.M. Pharr, An improved technique for determining hardness and elastic modulus using load and displacement senseing indentation experiments, Journal of Materials Research 7 (1992) 1564-1583.

[31] R. Drevet, H. Benhayoune, L. Wortham, S. Potiron, J. Douglade, D. Laurent-Maquin, Effects of pulsed current and H_2O_2 amount on the composition of electrodeposited calcium phosphate coatings, Materials Characterization 61 (2010) 786-795.

[32] D.T.M. Thanh, P.T. Nam, N.T. Phuong, L.X. Que, N. Van Anh, T. Hoang, T.D. Lam, Controlling the electrodeposition, morphology and structure of hydroxyapatite coating on 316L stainless steel, Materials Science and Engineering: C 33 (2013) 2037-2045.

[33] N. Ohtsu, S. Hiromoto, M. Yamane, K. Satoh, M. Tomozawa, Chemical and crystallographic characterizations of hydroxyapatite- and octacalcium phosphate-coatings on magnesium synthesized by chemical solution

deposition using XPS and XRD, Surface and Coatings Technology 218 (2013) 114-118.

[34] R.M. Wilson, J.C. Elliott, S.E.P. Dowker, L.M. Rodriguez-Lorenzo, Rietveld refinements and spectroscopic studies of the structure of Ca-deficient apatite, Biomaterials 26 (2005) 1317-1327.

[35] D.J. Blackwood, K.H.W. Seah, Galvanostatic pulse deposition of hydroxyapatite for adhesion to titanium for biomedical purposes, Materials Science and Engineering: C 30 (2010) 561-565.

[36] A.C. Fischer-Cripps. Nanoindentation, Springer, New York, 2002.

[37] L.H. He, O.C. Standard, T. T.Y. Huang, B.A. Latella, M.V. Swain, Mechanical behaviour of porous hydroxyapatite, Acta Biomaterialia 4 (2008) 577-586.

[38] D. Esqué-de los Ojos, J. Zhang, J. Fornell, E. Pellicer, J. Sort, Nanomechanical behaviour of open-cell nanoporous metals: Homogeneous versus thickness-dependent porosity, Mechanics of Materials 100 (2016) 167-174.

[39] L. Fu, K.A. Khor, J.P. Lim, Processing, microstructure and mechanical properties of yttria stabilized zirconia reinforced hydroxyapatite coatings, Materials Science and Engineering: A 316 (2001) 46-51.

[40] A. Mejias, R.T. Candidato Jr., L. Pawłowski, D. Chicot, Mechanical properties by instrumented indentation of solution precursor plasma sprayed hydroxyapatite coatings: Analysis of microstructural effect, Surface and Coatings Technology 298 (2016) 93-102.

4.2 Synthesis of α-Fe_2O_3 and Fe-Mn oxide foams with highly tunable magnetic properties produced by replication from polyurethane templates

Open cell foams consisting of Fe and Fe-Mn oxides were prepared from metallic Fe and Mn powder precursors by the replication method using porous polyurethane templates. First, reticulated polyurethane templates were coated by slurry impregnation. The templates were thermally removed at 260 ºC and the debinded powders were sintered at 1000 ºC under N_2 atmosphere. The structure, morphology and magnetic properties were studied by scanning electron microscopy, X-ray diffraction and vibrating sample magnetometry, respectively. The obtained Fe and Fe-Mn oxide foams possess both high surface area and homogeneous open-cell structure. Hematite (α-Fe_2O_3) foams were obtained from the metallic iron slurry independently of the N_2 flow. On the contrary, the microstructure of the FeMn-based foams could be tailored by adjusting the N_2 flow. While the main phase for a N_2 flow rate of 180 L/h was α-Fe_2O_3, the predominant phase for high N_2 flow rates (e.g., 650 L/h) was Fe_2MnO_4. Accordingly, a linear magnetization *versus* field behavior was observed for the hematite foams, while clear hysteresis loops were obtained for the Fe_2MnO_4 foams. Actually, the saturation magnetization of the foams containing Mn increases from 5 emu/g to 52 emu/g when increasing the N_2 flow rate (i.e., the amount of Fe_2MnO_4). The obtained foams are appealing for a wide range of applications, such as electromagnetic absorbers, catalysts supports, thermal and acoustic insulation systems or wirelessly magnetically-guided porous objects in fluids.

4.2.1 Introduction

Reticulated sponges made of Polyurethane (PU) have been commercially available since 1950s [1]. The first attempts to transfer porous templates into ceramic (i.e., oxide) foams by the powder slurry replication method date from early 60's [2]. At present, the method has become widely available for many applications involving porous oxide materials: electromagnetic wave absorption, gas sensors, catalysts, oil-water separation and lithium-ion batteries [3-8]. As a consequence, the polymeric sponge replication process has consolidated as a promising technique to create cellular oxide structures with 3D interconnected pores with high strength and acid and alkali resistance [9-11]. In the 70s, metallic foams started to be also prepared by this method and they found applications as battery electrodes, catalysts or filters [12-14]. Over the past ten years the replication method has been extended to manufacture porous steels [15-18], Cu-based [19] and titanium alloys [20, 21].

While many studies have focused on metallic foams [15-21], fewer efforts have been devoted recently to synthesize inorganic oxide foams through the polymer sponge replication process [22]. So far, the possibility to use this technique to produce oxide foams with magnetic properties has not been explored.

Manganese ferrite ($MnFe_2O_4$) is a well-known ceramic compound with electrically insulating and soft ferrimagnetic properties at room temperature. It has been widely used in the electronics industry to fabricate magnetic cores for read/write heads for high-speed tape or hard disk recording [23, 24]. More recently, $MnFe_2O_4$ has emerged as a promising material to be used as a catalyst [25, 26], in hydrogen production technologies [24] or for oil-water separation [7]. Diverse preparation techniques, such as high energy ball milling [24, 27], co-precipitation method [28, 29] or sol-gel routes [30], have been used to obtain $MnFe_2O_4$ powders and nanoparticles. However, the preparation of porous $MnFe_2O_4$ remains challenging and rather elusive.

Meanwhile, magnetic foams made of Fe_2O_3, Fe_3O_4, Co or Ni are appealing since they combine the intrinsic properties of magnetic materials with the aforementioned advantages of the porous structures, constituting magnetic materials with high surface area, low density and high strength-to-weight ratio. For instance, ultralight Fe_2O_3/C foams produced using polyelectrolyte-grafted PU sponges [7] exhibit one of the highest oil-absorption capacities among the reported counterparts. Magnetic nano-particles Fe_3O_4/polyurethane composites produced by *in-situ* blending methods have also been reported as good candidates for wastewater treatments, acting as carriers for immobilized microorganisms [31].

Therefore, the aim of the present work is to use the replication method to produce Fe and Fe-Mn oxides open-cell porous structures. The magnetic behavior of the foams is tuned, first, by the addition of Mn and, secondly, by adjusting the N_2 flow. The influence of the N_2 flow and the Mn content, as well as the synergic effect of porosity and magnetism are investigated.

4.2.2 Experimental

Commercial Fe (97%) and Mn (99%) powders were used to coat a reticulated polyurethane sponge by the impregnation method. First, the powders were mixed and mechanically milled in a planetary mill device (Fritsch Pulverisette 5) to reduce the powder size and to obtain the targeted composition, Fe or Fe-30Mn (nominal wt.%). The raw powders were milled under Ar atmosphere with a ball-to-powder weight ratio of 10:1 at 300 rpm for 15 h. To prepare the slurry, the milled powders were mixed with poly(ethylene glycol) and distilled water. The poly(ethylene glycol) acted as a binder and was used to control the slurry viscosity and to favor the adhesion of the powder particles to the sponge before sintering. The composition of the slurry is listed in Table 4.2.1.

Components	*Fe or Fe30Mn*	*Binder*	*distilled water*
Mass percent (%)	50	17	33

Table 4.2.1: Components and mass percentages of the slurry

Hence, 1 cm^3 of a commercial reticulated polyurethane sponge, acting as organic template, was immersed into the slurry for 5 min to allow complete impregnation. The sponge was removed from the suspension and was subsequently squeezed to ensure that only a thin layer of slurry covered the skeleton of the polyurethane template without blocking the pores. Then, the impregnated template was dried at room temperature for at least 12 hours before sintering. Finally, the template was thermally removed at 260 ºC and the debinded powders were sintered in a tubular furnace (Carbolite MTF 9/15) at 1000 ºC for 2 h under N_2 flow.

Scanning electron microscopy (SEM) observations were done on a Zeiss Merlin microscope equipped with an energy dispersive X-ray (EDX) spectroscopy detector for compositional analyses. X-ray diffraction (XRD) was carried out on a Philips X'Pert diffractometer using Cu K_α radiation. The measurements were performed in the angular range 2θ = 30–100° with a step size of 0.026°. Furthermore, Rietveld refinement of the XRD patterns using the X'Pert HighScore Plus software was carried out to determine the cell parameters and the percentage of the constituent phases.

Hysteresis loops were recorded at room temperature using a vibrating sample magnetometer (VSM) from MicroSense (LOT-QuantumDesign), with a maximum applied magnetic field of 20 kOe.

4.2.3. Results and discussion

4.2.3.1. Microstructure and compositional analyses

Figure 4.2.1 shows SEM images of the sintered open cell foams obtained by the replication process from Fe- (Figure 4.2.1a) and FeMn- (Figure 4.2.1 b-d) containing slurries. At first glance, a rather homogeneous pore distribution can be observed, with pore sizes in the order of 400 μm. Fully-compact pore walls were observed in the foams produced from the Fe- and FeMn- containing slurries at the lowest N_2 flow (Figure 4.2.1a and 4.2.1b); however, at larger N_2 flows, pore walls exhibit a nano-porous structure although the distribution and the size of the pores was not compromised. The composition of the foams obtained at different nitrogen flow rates, measured by energy-dispersive X-ray (EDX) analyses, is listed in Table 4.2.2. An O/Fe ratio of 1.56 is calculated for the foam produced from the Fe-containing slurry suggesting the formation of Fe_2O_3. It is worth mentioning that no changes were observed in the foams produced under larger N_2 flow (such as 350 L/h and 650 L/h) from the Fe-containing slurry in terms of pore morphology, integrity of the foam or chemical composition (not shown in the manuscript). However, the foams produced at open atmosphere were powdery and brittle. On the contrary, compositional changes were observed in the foams produced from the FeMn-containing slurry when changing the N_2 flow. For the foam produced at 180 L/h, the O/Fe(Mn) ratio is 1.5 suggesting the formation of Fe_2O_3 or $FeMnO_3$. Nonetheless, the O/Fe(Mn) ratio decreases to 1.38 and 1.27 suggesting the formation of $Fe_{3-x}(Mn)_xO_4$ as the N_2 flow is increased to 350 L/h and 650 L/h, respectively.

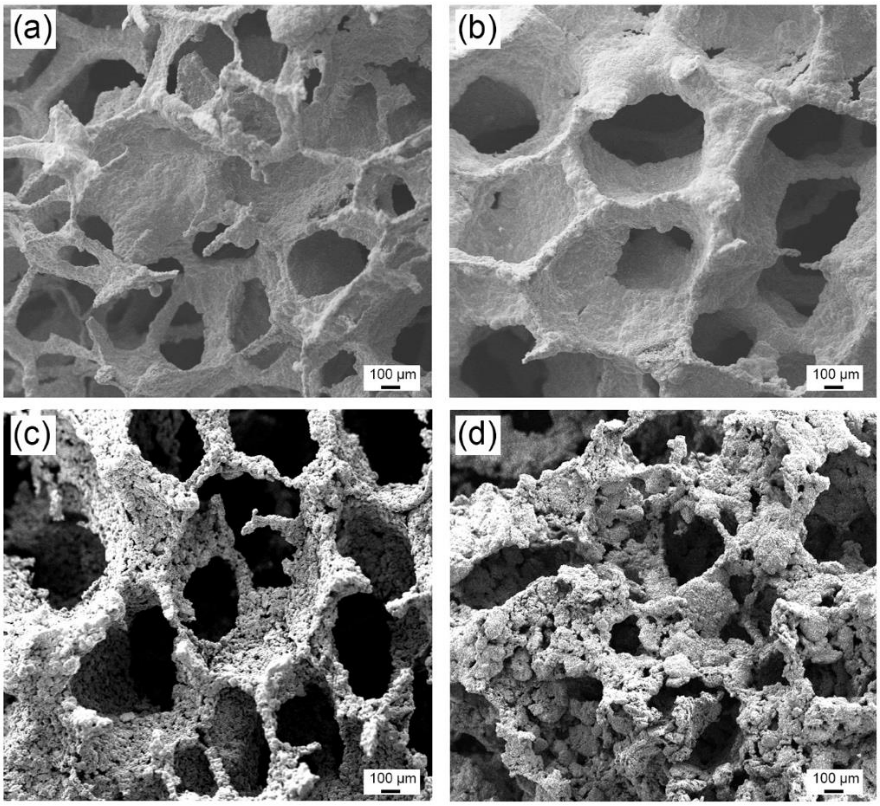

Figure 4.2.1: (a) SEM image of a Fe-O foam prepared at a nitrogen flow rate of 180 L/min. SEM image of Fe-Mn-O foams prepared under a nitrogen flow rate of (b) 180 L/h (c) 350 L/h and (d) 650 L/h.

Sample	Mn (at.%)	Fe (at.%)	O (at.%)
Fe-O (180 L/h)	0	39	61
Fe-Mn-O (180 L/h)	12	28	60
Fe-Mn-O (350 L/h)	16	26	58
Fe-Mn-O (650 L/h)	18	24	56

Table 4.2.2: EDX composition of the foams produced from the Fe-containing slurry at a N_2 flow of 180 L/h and from the FeMn-containing slurry at a N_2 flow of 180, 350 and 650 L/h.

To shed light on the microstructure of the open-cell foams X-ray diffraction was carried out (Figure 4.2.2). As suggested by EDX analyses, the foams produced from the Fe-containing slurry are composed of α-Fe_2O_3. On the contrary, the XRD of the foams produced from the FeMn-containing slurry are a mixture of α-Fe_2O_3, $FeMnO_3$ and Fe_2MnO_4 phases. Phase contributions and cell parameters estimated by Rietveld refinement are listed in Table 4.2.3. Sintering the FeMn-containing foams at higher N_2 flow results in larger amounts of Fe_2MnO_4. As can be observed in Table 4.2.3, the amount of Fe_2MnO_4 increases from 8.5 to 74 % when increasing the N_2 flow from 180 to 650 L/h. Accordingly, the Fe_2O_3 phase percentage decreases from 60 to 26 %. $FeMnO_3$ only forms under a N_2 flow of 180 L/h.

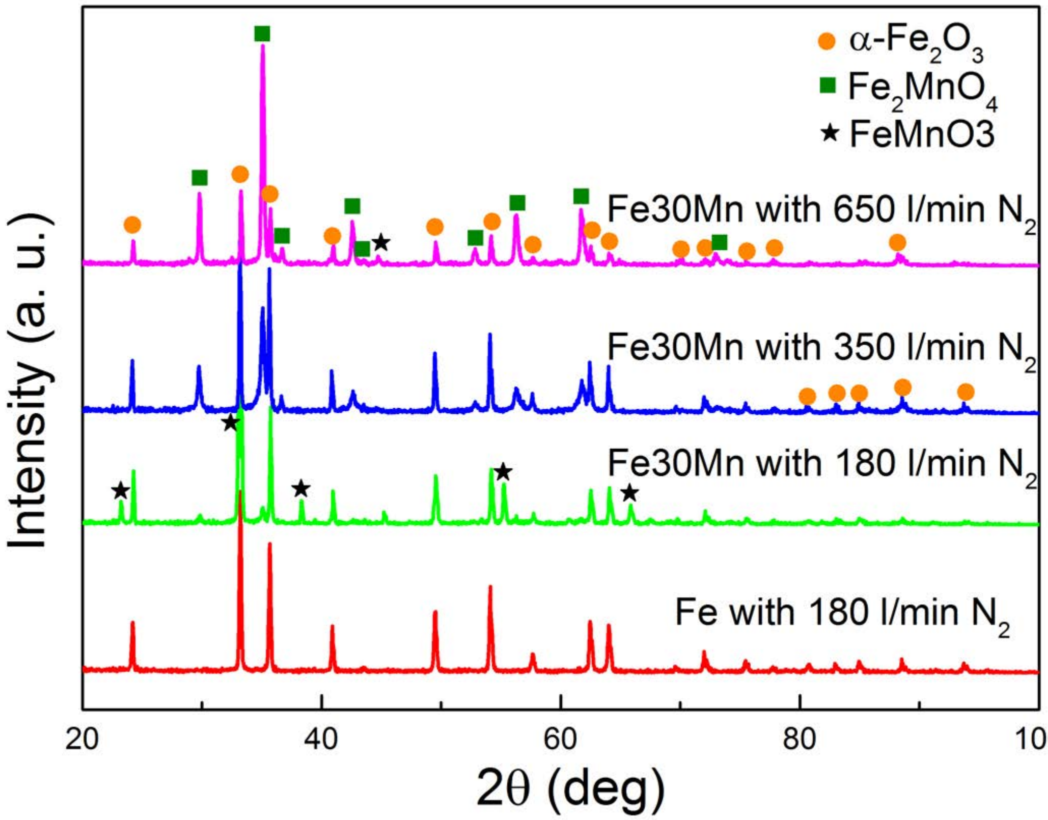

Figure 4.2.2: XRD patterns of the Fe-O foam produced at N_2 flow of 180 L/h and Fe-Mn-O foams produced at a N_2 flow of 180, 350 and 650 L/h.

Alloy	Phase		Cell parameters (Å)	%
Fe-O **(180 L/h)**	hematite	Fe_2O_3	*a* = 5.036; *c* = 13.748	100
Fe-Mn-O **(180 L/h)**	hematite	Fe_2O_3	*a* = 5.038; *c* = 13.741	60
	bixbyite	$FeMnO_3$	*a* = 9.417	31.5
	jacobsite	Fe_2MnO_4	*a* = 8.489	8.5
Fe-Mn-O **(350 L/h)**	hematite	Fe_2O_3	*a* = 5.036; *c* = 13.741	51
	jacobsite	Fe_2MnO_4	*a* = 8.483	49
Fe-Mn-O **(650 L/h)**	Hematite	Fe_2O_3	*a* = 5.036; *c* = 13.745	26
	jacobsite	Fe_2MnO_4	*a* = 8.5028	74

Table 4.2.3: Phase percentage and cell parameters of the obtained foams

4.2.3.2. Magnetic properties

Figure 4.2.3 shows the hysteresis loops of the open-cell porous foams produced from the Fe- and FeMn-containing slurries at different nitrogen flow rates. A linear magnetization versus field behavior (reaching 0.6 emu/g for an applied field of 20 kOe) was observed in the Fe-O foams, in agreement with the reported behavior for antiferromagnetic α-Fe_2O_3. Clear hysteresis loops are observed in the FeMn-containing foams as a result of the ferrimagnetic character of the Fe_2MnO_4 phase, which exhibits a theoretical saturation magnetization, M_s, of 77 emu/g [32]. The $FeMnO_3$ phase, present in the foam produced at a N_2 flow of 180 L/min, exhibits a weakly ferrimagnetic response with Ms ~ 0.23 emu/g [33]. Accordingly, the saturation magnetization of the FeMn-containing foams ranges from 5 emu/g to 52 emu/g depending on the amount of Fe_2MnO_4. For instance, an M_s value of 37.7 emu/g would be expected for a foam produced under a N_2 flow of 350 L/h as it contains 49 % of Fe_2MnO_4. The observed M_s in this case (40 emu/g) is in quite good agreement with the expected value. The foam produced under a N_2 flow of 650 L/h has Ms = 52 emu/g which is also in good agreement with the theoretically calculated value (57 emu/g).

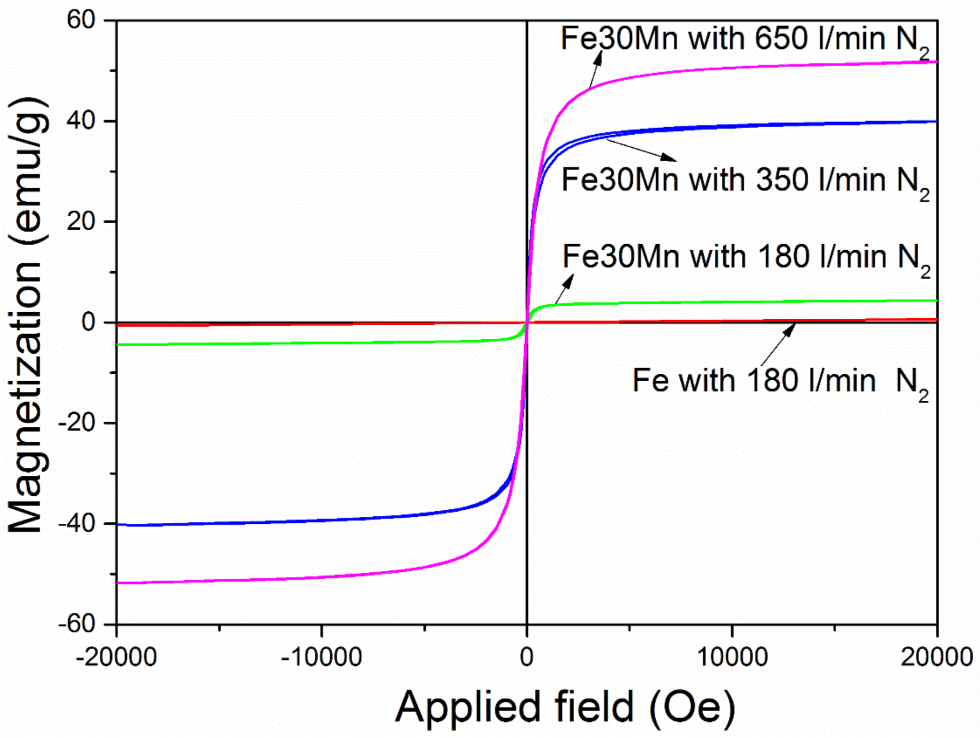

Figure 4.2.3: Hysteresis loops of four kinds of open-cell porous foams produced from the Fe- and FeMn-containing slurries at different nitrogen flow rate.

4.2.4 Conclusions

Highly porous foams with high surface area and homogeneous open-cell structure have been obtained by the replication process using polyurethane templates. The foams produced from the Fe-containing slurry consist of α-Fe_2O_3, independently of the N_2 flow. On the contrary, the phase composition of the foams produced from the FeMn-containing slurry can be tuned by adjusting the N_2 flow. The main phases of the Fe-Mn-O foams sintered under a N_2 flow of 180 L/h are α-Fe_2O_3 and $FeMnO_3$ with minor content of Fe_2MnO_4. Increasing the N_2 flow to 350 L/h results in a mixture of α-Fe_2O_3 and Fe_2MnO_4. The amount of manganese ferrite is further increased at a flow rate of 650 L/h. Hence, addition of Mn as well as the adjustment of the N_2 flow allows tailoring the magnetic response of the foams from practically non-magnetic to ferrimagnetic.

References

[1] R.B. Seymour, G.B. Kauffman, Polyurethanes: A Class of Modern Versatile Materials, Journal of Chemical Education 69 (1992) 909-910.

[2] S. Karl, A.V. Somers, Method of making porous ceramic articles, US Patents 309 0094, 1963.

[3] K.Y. Park, S.E. Lee, C.G. Kim, J.H. Han, Fabrication and electromagnetic characteristics of electromagnetic wave absorbing sandwich structures, Composites Science and Technology 66 (2006) 576-584.

[4] Z.P. Chen, C. Xu, C.Q. Ma, W.C. Ren, H.M. Cheng, Lightweight and flexible graphene foam composites for high-performance electromagnetic interference shielding, Advanced Materials 25 (2013) 1296-1300.

[5] F. Yavari, Z.P. Chen, A.V. Thomas, W.C. Ren, H. M. Cheng, N. Koratkar, High sensitivity gas detection using a macroscopic three-dimensional graphene foam network, Scientific Reports1 (2011) 166

[6] F.C. Buciuman, B. K. Czarnetzki, Preparation and characterization of ceramic foam supported nanocrystalline zeolite catalysts, Catalysis Today 69 (2001) 337-342.

[7] N. Chen, Q. Pan, Versatile fabrication of ultralight magnetic foams and application for oil-water separation, ACS Nano 7 (2013) 6875-6883.

[8] E. Kang, Y.S. Jung, A.S. Cavanagh, G.H. Kim, S.M. George, A.C. Dillon, J.K. Kim, J. Lee, Fe_3O_4 nanoparticles confined in mesocellular carbon foam for high performance anode materials for lithium-ion batteries, Advanced Functional Materials 21 (2011) 2430-2438.

[9] E.J.A.E. Williams, J.R.G. Evans, Expanded ceramic foam, Journal of Materials Science 31 (1996) 559-563.

[10] S.R. Wang, H.R. Geng, L.H. Hui, Y.Z. Wang, Reticulated porous multiphase ceramics with improved compressive strength and fracture

toughness, Journal of Materials Engineering and Performance 16 (2007) 113-118.

[11] S.B. Bhaduri, Science and technology of ceramic foams, Advanced Performance Materials1 (1994) 205-220.

[12] F.C. Arrance, Battery electrode and battery, and process for preparing said electrode, US Patent 3287 166, 1966.

[13] V.N. Antsiferov, A.M. Makarov, V.D Khramtsov, High-porosity permeable cellular metals and alloys in catalytic processes of gas cleaning, Advanced Engineering Materials 7 (2005) 77-91.

[14] J.F. Roesler, Application of polyurethane foam filters for respirable dust separation, Journal of the Air Pollution Control Association 16 (1966) 30-34.

[15] D.P. Haack, K.R. Butcher, T. Kim, T.J. Lu, Novel lightweight metal foam heat exchangers, in processing of ASME Int. Mechanical Congress, New York, 2001.

[16] P. Quadbeck, G. Stephani, K. Kümmel, J. Adler, G. Standke, Synthesis and properties of open-celled metal foams, Materials Science Forum, 534-536 (2007) 1005-1008.

[17] P. Quadbeck, K. Kümmel, R. Hauser, G. Standke, J. Adler, G. Stephani, Open cell metal foams-application-oriented structure and material selection, in processing of International Conference on Cellular Materials, CellMat 2010, Dresden, 279-288.

[18] P. Quadbeck, K. Kümmel, R. Hauser, G. Standke, J. Adler, G. Stephani, B. Kieback, Structural and material design of open-cell powder metallurgical foams, Advanced Engineering Materials 13 (2011) 1024-1030.

[19] H. Zhang, D. Pinjala, Y.K. Joshi, T.N. Wong, K.C. Toh, M.K. Iyer, Fluid flow and heat transfer in liquid cooled foam heat sinks for electronic packages, IEEE Transactions on Components and Packaging Technologies 28 (2005) 272-280.

[20] J.P. Li, S.H. Li, K.D. Groot, P. Layrolle, Improvement of porous titanium with thicker struts, Key Engineering Materials 240-242 (2003) 547-550.

[21] A. Manonukul, M. Tange, P. Srikudvien, Rheological properties of commercially pure titanium slurry for metallic foam production using replica impregnation method, Powder Technology 266 (2014) 129-134.

[22] P. Biswas, P. Ramavath, C.M. Nair, M.B. Suresh, N. Ravi, R. Johnson, Quasi-static compression behavior of nickel oxide, nickel oxide: zirconia, nickel:zirconia and nickel foams, Ceramics International 42 (2016) 10572-10578.

[23] X. Zuo, B. Barbiellini, C. Vittoria, Calculation of exchange constants in manganese ferrite ($MnFe_2O_4$), Journal of Magnetism and Magnetic Materials 272 (2004) 306-311.

[24] F. Padella, C. Alvani, A. L. Barbera, G. Ennas, R. Liberatore, F. Varsano, Mechanosynthesis and process characterization of nanostructured manganese ferrite, Materials Chemistry and Physics 90 (2005) 172-177.

[25] F.G. Durán, B.P. Barbero, L.E. Cadús, C. Rojas, M.A. Centeno, J.A. Odriozola, Manganese and iron oxides as combustion catalysts of volatile organic compounds, Applied Catalysis B: Environmental 92 (2009) 194-201.

[26] M.M.B. Quiroga, B.P. Barbero, L.E. Cadus, Synthesis of a catalyst of Mn–Fe–O by mechano-chemical reaction, Applied Catalysis A: General 474 (2014) 26-33.

[27] M.H. Mahmoud, H.H. Hamdeh, J.C. Ho, M.J. O’shea, J.C. Walker, Mössbauer studies of manganese ferrite fine particles processed by ball-milling, Journal of Magnetism and Magnetic Materials 220 (2000) 139-146.

[28] J. Amighian, M. Mozaffari, B. Nasr, Preparation of nano-sized manganese ferrite ($MnFe_2O_4$) via coprecipitation method, Physica Status Solidi (C) 3 (2006) 3188-3192.

[29] M. Baldi, V.S. Escribano, J.M.G. Amores, F. Milella, G. Busca, Characterization of manganese and iron oxides as combustion catalysts for propane and propene, Applied Catalysis B: Environmental 17 (1998) L175-L182.

[30] W.H. Kwon, J.Y. Kang, J.G. Lee, S.W. Lee, K.P. Chae, Synthesis and magnetic properties of Zn, Co and Ni substituted manganese ferrite powders by sol-gel method, Journal of Magnetics 15 (2010) 159-164.

[31] L.C. Zhou, G.Y. Li, T.C. An, Y.F. Li, Synthesis and characterization of novel magnetic Fe_3O_4/polyurethane foam composite applied to the carrier of immobilized microorganisms for wastewater treatment, Research on Chemical Intermediates 36 (2010) 277-288.

[32] M.Y. Rafique, P.L. Qing, Q.U.A. Javeb, M.Z. Iqbal, Q.H. Mei, M.H. Farooq, G.Z. Gang, M. Tanveer, Growth of monodisperse nanospheres of $MnFe_2O_4$ with enhanced magnetic and optical properties, Chinese Physics B 22 (2013) 107101.

[33] S. Rayaprol, S.D. Kaushik, P.D. Babu, V. Siruguri, Structure and magnetism of $FeMnO_3$, AIP Conference Proceedings 1512 (2013) 1132-1133.

5. General discussion

Chapter 5: General discussion

Chapter 5: General discussion

Given the exceedingly fast degradation rates of Mg-based biodegradable alloys and the relatively low strength of biodegradable polymers, this Thesis aimed at developing Fe-based alloys that could be at the same time biodegradable and exhibit outstanding mechanical properties and biomechanical compatibility. Previous works from the literature had shown that the Fe-Mn system (with eventual addition of Pd) could fulfill both requirements. Moreover, for sufficiently high Mn contents, these alloys became non-ferromagnetic, thus being appropriate for biomedical implants applications, where diagnosis techniques like MRI or NMR (whose results are prone to be influenced by spurious magnetic signals) are often required. Taking into consideration this conceptual framework, two quaternary Fe-based alloys with presumably improved properties were designed and subsequently prepared by arc melting followed by copper mold suction casting. These techniques were selected to optimize the mixture of all metallic elements (and hence achieve a homogeneous composition) while reducing the grain size which typically renders high hardness values. The addition of 1wt.% of Pd to the ternary Fe-30Mn-6Si was expected to increase its degradation rate because of the formation of small and homogeneously dispersed Pd-rich precipitates, which were indeed observed by electron microscopy. In turn, the addition of 6 wt.% of Si to the ternary Fe-10Mn-1Pd, besides increasing the strength of the alloy, it was expected to eventually aid the healing process and to help the immunologic system, as silicon is an essential mineral in the human body. In previous works, only the binary Fe-Mn and ternary Fe-Mn-Si and Fe-Mn-Pd alloys had been investigated and, hence, the idea of our work was to produce quaternary alloys that could take advantage of all the aforementioned properties in a synergetic manner. Since the Fe-30Mn6Si1Pd alloy was found to be non-ferromagnetic and exhibit the appropriate transformation temperature and microstructure, it might be used as self-expandable stents taking advantage of the superelasticity effect, thus minimizing the risk of damaging the vascular tissue due to inflammation reactions produced by the balloon expansion in conventional stenting procedures that employ non-superelastic materials. This alloy could also find applications as orthopedic implants. However, the biodegradation of this material was found to be hampered by the formation of surface corrosion products. Thus, at least in static immersion conditions and in its fully dense form, the alloy cannot be considered to be truly biodegradable. Introduction of porosity and/or using this material in dynamic conditions (moving bodily fluids) could be two strategies to enhance the observed degradation rates. Remarkably, this alloy, in its bulk, fully-dense form, was not cytotoxic.

Similarly, the Fe-10Mn6Si1Pd alloy was not found to be fully biodegradable and, in addition, it exhibited a clear ferromagnetic behavior, which would preclude its use for biomedical implant applications. Nonetheless, given its non-cytotoxic characteristics, this alloy could be used as a building block in magnetically (wirelessly)-actuated microrobots platforms (e.g., for drug delivery or biological labeling, if properly functionalized and combined with drugs or photoluminescent materials).

An aspect of interest from our studies is that while indirect studies performed in the presence of the Fe-10Mn6Si1Pd alloy showed that this material is not cytotoxic by itself, cracking and oxide formation (stemming from surface corrosion) hinder cell adhesion and proliferation. Conversely, Fe-30Mn6Si1Pd can be considered as cytocompatible because Saos-2 cells can adhere and proliferate on its surface and the alloy is non-hemolytic. This further demonstrates the potential of the Fe-30Mn6Si1Pd for bioimplant applications.

In terms of biomechanical compatibility, one of the requirements to avoid stress shielding effect and provide good osseointegration is to use materials with a Young's modulus close to that of the human bone (from 3-20 GPa). The formation of porous oxide layers at the surface of the investigated alloys results in relatively low Young's modulus, not far from that of bone. As degradation takes place slowly (complete degradation of the implant might be expected at 24 months) the absence of mismatch between the bone and the implant is necessary. Interestingly, our results reveal that the progressive degradation of the alloys is accompanied with a reduction of Young's modulus, hence enhancing the mechanical compatibility. Furthermore, porosity could be expected to also improve osseointegration, as the bone can grow inside the pores, while also accelerating the slow degradation rates.

To tackle these issues, porous Fe-30Mn6Si1Pd alloys were prepared by a simple press and sinter process from ball-milled Fe, Mn, Si and Pd powders blended with 10 wt.%, 20 wt.% and 40 wt.% NaCl. A carefull design of the alloy's composition is required to avoid ferromagnetic properties during the whole degradation process which, as aforementioned, would hinder the utilization of NMR or MRI techniques, required to monitor the patient's recovery after surgery. Our results on this porous alloy reveal that both hardness and Young's modulus tend to increase for immersion periods up to 14 days (probably because of the formation of mechanically-hard corrosion products like oxides and hydroxides which progressively tend to fill the pores). However, for longer immersion times, the structural coherence reduces, resulting in lower Young's modulus. Remarkably, E_r of all the porous alloys reaches values close to 20 GPa after long-term immersion, a value which is close to the Young's modulus of human bones (3–27 GPa), hence favoring good biomechanical compatibility between an eventual implant and the neighboring bone tissue. Furthermore, porosity increases the overall available surface area of the material to the corrosive environment and, at the same time, acts as defects, thereby enhancing the degradation of the specimens. However, this porous Fe-based material faces the challenge of allowing for cell viability and proliferation. The high corrosion and degradation rates of the porous disks' surface causes thin layers of material to quickly detach from the alloys surface, preventing cell adhesion during the first 24 h of culture and precluding the assessment of cytotoxicity in cells growing directly onto the alloys. For this reason, indirect tests in conditioned medium were used to assess cytotoxicity. While the bulk alloy was clearly not cytotoxic, neither in terms of cell viability nor in terms of cells proliferation, the Fe-30Mn6Si1Pd-40%NaCl had a cytotoxic effect. This toxicity is mainly due to the fast ion release from the porous alloy compared to the bulk one.

In order to improve the biocompatibility of the Fe-Mn-Si-Pd system, we deposited brushite and hydroxyapatite coatings on the surface of a Fe-10Mn-

6Si-1Pd alloy. Preliminary results on the formation of these layers by electrodeposition (not previously attempted in the literature onto Fe-based alloys) revealed that oriented hydroxyapatite nanoplates could be directly grown by electrodeposition with no need of subsequent thermal or solution treatments. The obtained results make the coated FeMnSiPd alloys potential candidate materials to be utilized in the biomedical field. However, one of the drawbacks of the electrodeposited coatings when compared to those obtained by other synthesis techniques (e.g., sputtering, plasma spraying, laser deposition) is their relatively bad adhesion to the substrate. To overcome this drawback, pulsed current electrodeposition was used instead of direct current electrodeposition. The adhesion of the coatings, evaluated by scratch tests, was significantly better and delamination or failure were not detected. In addition, by tuning the deposition time and the composition of the bath, coatings with different amounts of brushite and HAp phases could be obtained. Electrodeposition of these coatings generally resulted in needle-, rod- or plate-like morphologies leading to porous structures. As a result, the measured Young's modulus and hardness are lower than those of fully-dense coatings with analogous compositions, hence again approaching the values of both parameters to those of cortical bone.

During the process of attempting to increase the porosity of Fe-based alloys, we found that pronounced oxidation took place at the surface of these alloys. To extend these results, we developed a new procedure to purposely obtain Fe and Fe-Mn oxides open cell foams from metallic Fe and Mn powder precursors by the replication method using porous polyurethane templates. The obtained foams could be appealing for a wide range of applications, such as electromagnetic absorbers, catalysts supports, thermal and acoustic insulation systems or wirelessly magnetically-guided porous objects in fluids. Fe or Fe-30Mn oxides were selected as target compositions. Magnetic characterization revealed that antiferromagnetic hematite (α-Fe_2O_3) foams were obtained from the metallic iron slurry independently of the N_2 flow. However, the saturation magnetization of the foams containing Mn increased from 5 emu/g to 52 emu/g when increasing the N_2 flow rate (i.e., the amount of Fe_2MnO_4). Hence, addition of Mn as well as the adjustment of the N_2 flow allows tailoring the magnetic response of the foams from practically non-ferrimagnetic to ferrimagnetic.

Still dealing with magnetic properties, further experimental work was also performed to adjust the surface state of non-magnetic Fe-based metallic glasses. We applied the FSPLI method to create periodic magnetic patterns at the surface of a non-ferromagnetic amorphous Fe-based alloys. The origin of the observed ferromagnetism is the FSPLI-induced surface devitrification of the non-magnetic amorphous steel. Among the various generated crystalline phases were ferromagnetic α-Fe and Fe_3C, and ferrimagnetic $(Fe,Mn)_3O_4$ and Fe_2CrO_4. The occurrence of periodic arrays of submicron magnetic structures was evidenced both by magnetometry measurements and by magnetic force microscopy imaging. In addition, much smaller nanoripples (of a few tens of nm in lateral size) were also generated during the FSPLI process, which is consistent with the coupling of the incident electromagnetic radiation with plasmon charge oscillations. Besides magnetic aspects, this topological surface modification is also appealing for other practical applications, since it has been reported to cause an increase of the corrosion resistance of steel, to induce superhydrophobicity in several alloys and to improve the intrinsic plasticity in certain types of metallic glasses. Both the generated ferromagnetism and the resulting tribological/adhesion properties could make it possible to use this material for biological and magnetic recording applications.

Besides all these aforementioned applications, porous Fe-based alloys could also be employed in environmental healing technologies. Fully nanoporous Fe-rich alloy, prepared by selective dissolution of melt-spun $Fe_{43.5}Cu_{56.5}$ ribbons, was prepared to be an excellent heterogeneous Fenton catalyst towards the degradation of MO in aqueous solution. This material was also ferromagnetic and could thus be wirelessly manipulated towards specific locations within polluted wastewater. Remarkably, the effectiveness of this nanoporous material surpassed the results obtained from homogeneous Fenton reaction using an equivalent concentration of Fe cations released into the media from the nanoporous alloy. The different factors that promoted the observed high catalytic activity (i.e., the enhanced surface area stemming from the nanoporosity, the ability of this material to generate surface hydroxyl radicals, the regeneration of Fe^{2+} at its surface, and the sustained release of ferrous ions into the solution) have been thoroughly discussed in this Thesis. One weak point of this kind of material is the recyclability as the leaching of Fe ions during the Fenton reaction causes irreversible modifications in the material.

In summary, from a very general perspective, this Thesis tackles different synthetic approaches to obtain Fe-based multifunctional alloys, mainly focusing on biomedical and environmental applications (hence going beyond the conventional structural applications of Fe-based alloys like steels), and with emphasis on the design of composition and morphology to tailor both the mechanical and magnetic properties of the resulting materials. Non-conventional material architectures, like porous foams or 3D interconnected metal nanoporous framework, prepared by different approaches, are shown to be appealing to achieve specific target properties which cannot be easily accomplished with current Fe-based alloys.

6. Conclusions

Chapter 6: Conclusions

The following conclusions can be drawn from this Thesis:

- Two new Fe-based alloys, Fe-10Mn6Si1Pd and Fe-30Mn6Si1Pd, have been fabricated by arc melting followed by copper mold suction casting. Compared with the ferromagnetic Fe-10Mn6Si1Pd alloy, Fe-30Mn6Si1Pd remains non-ferromagnetic even after long-term immersion, hence allowing its use in the orthopedic field because of the compatibility with NMR and MRI techniques. Both Fe-10Mn6Si1Pd and Fe-30Mn6Si1Pd alloys exhibit larger hardness and lower Young's modulus compared to other Fe-based materials (e.g. austenitic steels). In terms of biocompatibility, the more hydrophilic character of the Fe-10Mn6Si1Pd alloy favors the initial cell adhesion. However, the formation of a cracked, loosely attached, oxide layer in this case, facilitates a pronounced ion release, hence hampering cell proliferation on the surface of this alloy to some extent. On the contrary, the Fe-30Mn6Si1Pd alloy shows good cell proliferation.

- By increasing the amount of NaCl from 10 to 40 wt.%, the porosity of the Fe-30Mn6Si1Pd alloys increases and the Young's modulus decreases from 55 GPa to 7 GPa, hence matching the Young's modulus of human bone (i.e., enhancing biomechanical compatilibity). Furthermore, Fe-30Mn6Si1Pd alloys produced from 10 wt.% and 20 wt.% NaCl cannot be considered to be cytotoxic. However, alloy produced from 40 wt.% NaCl has a strong cytotoxic effect from day 3 of cell culture. Hence, the faster and higher corrosion and ion release from highly porous specimens compromise the biocompatibility of this highly porous alloy.

- Porous CaP coatings with different amounts of brushite and HAp phases onto Fe-10Mn6Si1Pd substrates have been prepared by pulsed current electrodeposition. Because of the porous morphology of the coatings, the measured Young's modulus and hardness are lower than those of fully-dense coatings with analogous compositions, hence approaching the values of both parameters to those of cortical bone. Delamination or failure of the coatings were not detected during scratch tests, thus corroborating the good adherence of the coatings to the Fe-based alloy surface.

- Highly porous Fe and Fe-Mn oxides foams with high surface area have been obtained by the replication process using polyurethane templates. The results reveal that antiferromagnetic hematite (α-Fe_2O_3) foams are obtained from the Fe-containing slurry independently of the N_2 flow. However, the saturation magnetization of the foams containing Mn increases from 5 emu/g to 52 emu/g when increasing the N_2 flow rate from 180 L/h to 650 L/h. Hence, addition of Mn as well as the adjustment of the N_2 flow allows tailoring the magnetic response of the foams from practically non-magnetic to soft ferrimagnetic.

- Fully nanoporous Fe-rich ribbons have been obtained by selective dissolution of the fcc-Cu phase from phase-separated $Fe_{43.5}Cu_{56.5}$ ribbons. These nanoporous ribbons are very efficient in degrading MO in an aqueous solution at pH 3, thus acting as an efficient heterogeneous Fenton catalyst. The ferromagnetic properties of these dealloyed ribbons can be used to magnetically guide them toward specific locations in polluted water tanks to degrade organic matter.

- FSPLI was used to form periodic ripple and nanoripple patterns of sub-micrometer-sized magnetic structures at the surface of non-ferromagnetic amorphous steel. The occurrence of the ferromagnetic properties is associated with the laser-induced devitrification of the glassy structure to form ferromagnetic (α-Fe and Fe_3C) and ferrimagnetic [$(Fe,Mn)_3O_4$ and Fe_2CrO_4] phases. Nanoripples are consistent with the coupling of the incident electromagnetic radiation with plasmon charge oscillations. The observed variations in adhesion force can be particularly important for certain applications like traps for magnetic nanoparticles, where an exceedingly hydrophobic surface would not be desirable.

7. Future perspectives

Chapter 7: Future perspectives

New promising future perspectives are envisaged based on the results achieved in this Thesis. In the following, issues which deserve more attention in the near future are briefly summarized:

- The preliminary degradation tests carried out in the fully-compact Fe-based alloys seem to point out that the degradation rate of these alloys might still be too slow. To ensure that these materials could be used as real biodegradable implants, more detailed studies (i.e. dynamic immersion tests, in-vivo experiments, long-term degradation tests) should be carried out. Other methodologies could also be considered to further improve the degradation rate of these Fe-based alloys, such as addition of a second phase, surface modification or the use of other processing methods.
- It has been proved that the introduction of different degrees of porosity enhances the mechanical compatibility between an eventual implant and the neighboring bone tissue (section 3.2). The influence of the pore shape and size on the resulting mechanical properties, cell adhesion and proliferation response could also be explored. Other porogens (different than NaCl) could be used for such a purpose.
- Electrodeposition has been proved to be useful to grow brushite and HAp coatings at the surface of Fe-based alloys. The cellular response onto these coatings (so far grown on Fe-10Mn6Si1Pd alloy) remains unexplored. Cell adhesion and cell proliferation tests could be carried out. Potentiodynamic polarization studies and ion release experiments could also be performed to determine the corrosion rates of the CaP-coated Fe-based alloy.
- Either annealing of the as-sintered Fe-Mn-O foams or sintering in H_2-containing atmosphere could be implemented to obtain single phase Fe_2MnO_4 with larger ferrimagnetic response or even the metallic Fe-Mn

phase. Additional experiments could be carried out to test their performance as catalysts.

- The influence of voltage, temperature and time on the composition of dealloyed FeCu ribbons can be further studied. Extrapolation to bulk FeCu and sputtered FeCu thin films could be explored to obtain bulk nanoporous alloys or nanoporous thin films for diverse applications.

Chronogram and scientific curriculum

A chronogram of the work is shown as follows:

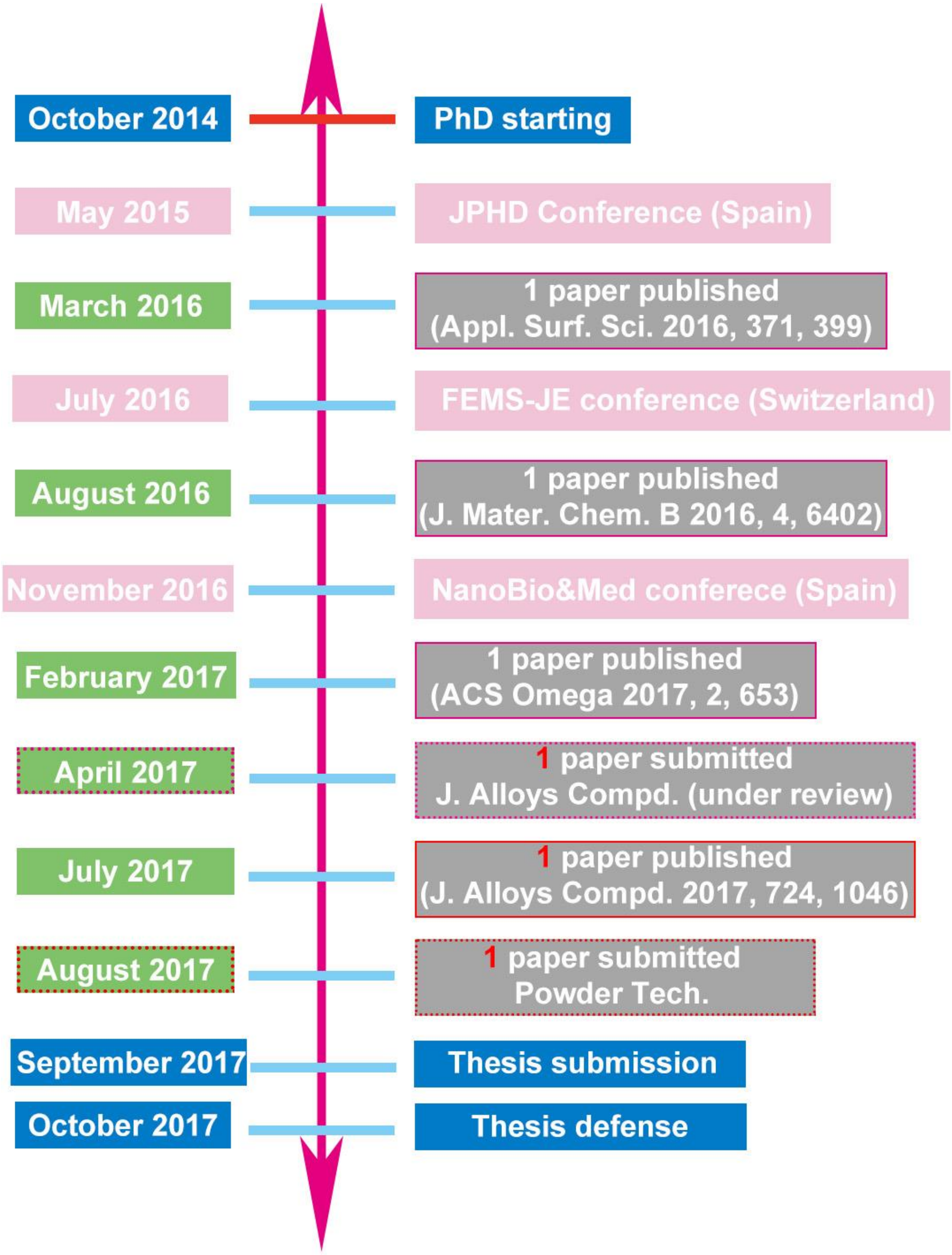

Publications

1. **Y.P. Feng**, A. Blanquer, J. Fornell, H.Y. Zhang, P. Solsona, M.D. Baró, S. Suriñach, E. Ibáñez, E. García-Lecina, X.Q. Wei, R. Li, L. Barrios, E. Pellicer, C. Nogués, J. Sort, Novel Fe-Mn-Si-Pd alloys: insights into mechanical, magnetic, corrosion resistance and biocompatibility performances, **J. Mater. Chem. B 2016**, 4, 6402-6412. (SCI, IF: 4.543)
2. **Y.P. Feng**, N. Gaztelumendi, J. Fornell, H.Y. Zhang, P. Solsona, M.D. Baró, S. Suriñach, E. Ibáñez, L. Barrios, E. Pellicer, C. Nogués, J. Sort, Mechanical properties, corrosion performance and cell viability studies on newly developed porous Fe-Mn-Si-Pd alloys, **J. Alloys Compd. 2017**, 724, 1046-1056. (SCI, IF: 3.133)
3. H.Y. Zhang, **Y.P. Feng**, D. Nieto, E. García-Lecina, C. Mcdaniel, J. Díaz-Marcos, M.T. Flores-Arias, G.M. O'connor, M.D. Baró, E. Pellicer, J. Sort, Sub-micron magnetic patterns and local variations of adhesion force induced in non-ferromagnetic amorphous steel by femtosecond pulsed laser irradiation, **Appl. Surf. Sci. 2016**, 371, 399-406. (SCI, IF: 3.387)
4. **Y.P. Feng**, L. Zhang, R.X. Ke, Q.L. Wan, Z. Wang, Z.H. Lu, Thermal stability and oxidation behavior of AlTiN, AlCrN and AlCrSiWN coatings, **Int. J. Refract. Met. H. 2014**, 43, 241-249. (SCI, IF: 2.155)
5. L. Zhang, **Y.P. Feng**, Q. Nan, R.X. Ke, Q.L. Wan, Z. Wang, Effects of titanium-based raw materials on electrochemical behavior of Ti(C,N)-based cermets, **Int. J. Refract. Met. H. 2015**, 48, 11-18. (SCI, IF: 2.155)
6. H.Y. Zhang, **Y.P. Feng**, Y.Y. Cheng, M.D. Baró, A. Altube, E. García-Lecina, F. Alcaide, E. Pellicer, T. Zhang, J. Sort, Nanoporous Fe-based alloy prepared by selective dissolution: an effective Fenton catalyst for water remediation, **ACS Omega 2017**, 2, 653-662. (new Journal)
7. **Y.P. Feng**, J. Fornell, H.Y. Zhang, P. Solsona, M.D. Baró, S. Suriñach, E. Pellicer, J. Sort, Synthesis of α-Fe_2O_3 and Fe-Mn oxide foams with highly tunable magnetic properties by the replication method from polyurethane templates, **Powder Technol. 2017**. (submitted)
8. J. Fornell, **Y.P. Feng**, H.Y. Zhang, P. Solsona, M.D. Baró, S. Suriñach, E. Pellicer, J. Sort, Mechanical behaviour of brushite and hydroxyapatite

coatings electrodeposited on newly developed FeMnSiPd alloys, **Alloys Compd. 2017**. (revision submitted)

9. L. Zhang, **Y.P. Feng**, S. Chen, H.P. Wu, In situ formation of RE_2S_3 and RE_2O_2S phases on sinter skin of Cr-mischmetal co-doped WC-Co alloy, **T. Nonferr. Metal. Soc. 2014**, 24, 401-405. (SCI, IF: 1.342)
10. L. Zhang, Y. Chen, **Y.P. Feng**, S. Chen, Q.L. Wan, J.F. Zhu, Electrochemical characterization of AlTiN, AlCrN and AlCrSiWN coatings, **Int. J. Refract. Met. H. 2015**, 53, 68-73. (SCI, IF: 2.155)
11. L. Zhang, M.W. Xie, Q. Nan, **Y.P. Feng**, Z. Wang, Y.H. He, Transformation of cobalt gradient structure after resintering of DP cemented carbide, **Int. J. Refract. Met. H. 2013**, 38, 118-123. (SCI, IF: 2.155)
12. L. Zhang, S. Chen, Q. Nan, M.W. Xie, H.P. Wu, **Y.P. Feng**, Effect of La containing phases on microscopic wear characteristics and residual stress of WC-Co cemented carbide, **Int. J. Refract. Met. H. 2013**, 41, 7-11. (SCI, IF: 2.155)
13. L. Zhang, M.W. Xie, X. Cheng, Q. Nan, Z. Wang, **Y.P. Feng**, Micro characteristics of binder phases in WC-Co cemented carbides with Cr-V and Cr-V-RE additives, **Int. J. Refract. Met. H. 2013**, 36, 211-219. (SCI, IF: 2.155)

Contributions to Conferences

*** Presenting Author**

- **Y.P. Feng***, N. Gaztelumendi, J. Fornell, H. Y. Zhang, P. Solsona, M. D. Baró, S. Suriñach, E. Ibáñez, E. García-Lecina, L. Barrios, E. Pellicer, C. Nogués, J. Sort, Novel Fe-Mn-Si-Pd dense and porous alloys: insights on mechanical, magnetic and corrosion performance, *NanoBio&Med*, November 22-24th, **2016, Poster presentation.**
- **Y.P. Feng***, A. Blanquer, J. Fornell, H. Y. Zhang, P. Solsona, M. D. Baró, S. Suriñach, E. Ibáñez, E. García-Lecina, E. Pellicer, C. Nogués, J. Sort, Novel Fe-Mn-Si-Pd biocompatible alloys: mechanical, magnetic and

corrosion performance, *FEMS Junior Euromat*, July 10-14th, 2016, **Poster presentation.**

- **Y.P. Feng***, H. Y. Zhang, E. Pellicer, J. Sort, Novel, Mechanical and magnetic properties of biodegradable Fe-10Mn6Si1Pd and Fe-30Mn6Si1Pd alloys, *JPHD: 1st Scientific Meeting of BNC-b Students*, May 20-21st, **2015, Oral presentation.**